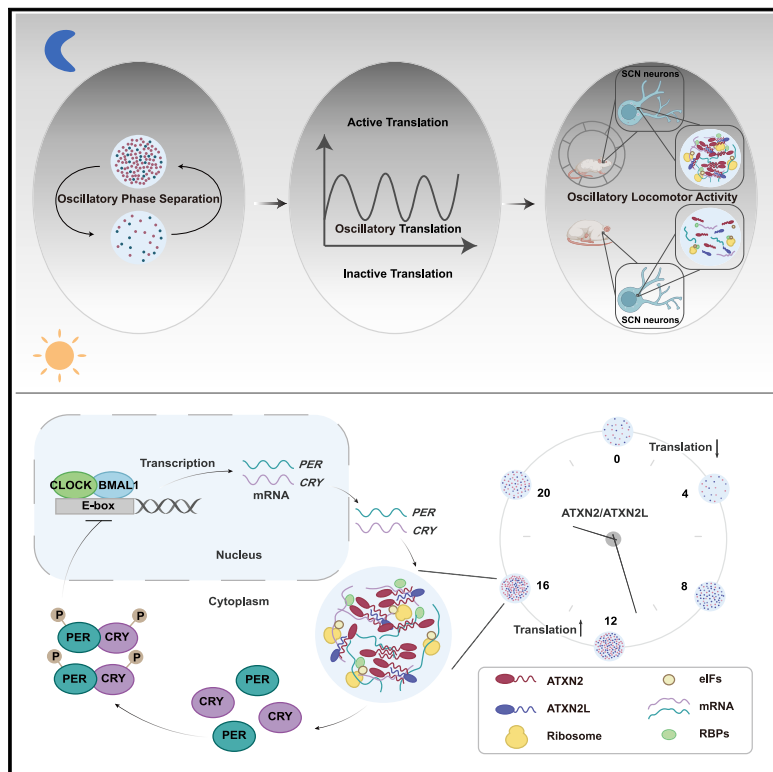


Circadian clocks are modulated by compartmentalized oscillating translation

Graphical abstract



Authors

Yanrong Zhuang, Zhiyuan Li,
Shiyue Xiong, ..., Yue Huang,
Xuerui Yang, Yi Lin

Correspondence

yangxuerui@tsinghua.edu.cn (X.Y.),
linyi@mail.tsinghua.edu.cn (Y.L.)

In brief

ATXN2 and ATXN2L condensates recruit ribosomes and selective mRNAs to regulate translation of key circadian clock genes.

Highlights

- ATXN2 and ATXN2L together modulate the mammalian circadian clock
- ATXN2/2L phase-separated condensates oscillate and regulate rhythmic translation
- ATXN2 condensates recruit ribosomes and selective mRNAs for translational activation
- *PER2* mRNAs are co-localized and translated within ATXN2 condensates in the SCN



Article

Circadian clocks are modulated by compartmentalized oscillating translation

Yanrong Zhuang,^{1,8} Zhiyuan Li,^{2,8} Shiyue Xiong,^{1,8} Chujie Sun,^{2,8} Boya Li,¹ Shuangcheng Alivia Wu,³ Jiali Lyu,¹ Xiang Shi,⁴ Liang Yang,⁵ Yutong Chen,¹ Zhangbin Bao,¹ Xi Li,¹ Chuhanwen Sun,¹ Yuling Chen,² Haiteng Deng,² Tingting Li,⁵ Qingfeng Wu,⁴ Ling Qi,³ Yue Huang,^{6,7} Xuerui Yang,^{2,*} and Yi Lin^{1,9,*}

¹State Key Laboratory of Membrane Biology, IDG/McGovern Institute for Brain Research, Tsinghua-Peking Joint Centre for Life Sciences, School of Life Sciences, Tsinghua University, Beijing 100084, China

²School of Life Sciences, MOE Key Laboratory of Bioinformatics, Center for Synthetic & Systems Biology, Tsinghua University, Beijing 100084, China

³Department of Molecular & Integrative Physiology, Division of Metabolism, Endocrinology & Diabetes, Department of Internal Medicine, University of Michigan Medical School, Ann Arbor, MI 48105, USA

⁴State Key Laboratory of Molecular Development Biology, Institute of Genetics and Developmental Biology, Chinese Academy of Sciences, Beijing 100101, China

⁵Department of Medical Bioinformatics, School of Basic Medical Sciences, Key Laboratory for Neuroscience, Ministry of Education, National Health Commission of China, Peking University, Beijing 100191, China

⁶China National Clinical Research Center for Neurological Diseases and Department of Neurology, Beijing Tiantan Hospital, Capital Medical University, Beijing 100050, China

⁷Pharmacology Department, School of Biomedical Sciences, Faculty of Medicine, UNSW Sydney, Sydney, Australia

⁸These authors contributed equally

⁹Lead contact

*Correspondence: yangxuerui@tsinghua.edu.cn (X.Y.), linyi@mail.tsinghua.edu.cn (Y.L.)

<https://doi.org/10.1016/j.cell.2023.05.045>

SUMMARY

Terrestrial organisms developed circadian rhythms for adaptation to Earth's quasi-24-h rotation. Achieving precise rhythms requires diurnal oscillation of fundamental biological processes, such as rhythmic shifts in the cellular translational landscape; however, regulatory mechanisms underlying rhythmic translation remain elusive. Here, we identified mammalian ATXN2 and ATXN2L as cooperating master regulators of rhythmic translation, through oscillating phase separation in the suprachiasmatic nucleus along circadian cycles. The spatiotemporal oscillating condensates facilitate sequential initiation of multiple cycling processes, from mRNA processing to protein translation, for selective genes including core clock genes. Depleting ATXN2 or 2L induces opposite alterations to the circadian period, whereas the absence of both disrupts translational activation cycles and weakens circadian rhythmicity in mice. Such cellular defect can be rescued by wild type, but not phase-separation-defective ATXN2. Together, we revealed that oscillating translation is regulated by spatiotemporal condensation of two master regulators to achieve precise circadian rhythm in mammals.

INTRODUCTION

Living organisms exhibit a self-sustained circadian rhythm of approximately 24 h, owing to Earth's rotation. Many crucial behavioral and physiological functions cycle in response to circadian rhythm. In most mammals, circadian rhythm is generally controlled by a hierarchical network of central and peripheral pacemakers, among which the suprachiasmatic nucleus (SCN) in the anterior hypothalamus serves as the principal circadian clock of the brain.¹ The SCN entrains to external zeitgebers and transmits clock information to downstream peripheral controllers in other brain regions or peripheral tissues.

At the molecular level, a group of "clock genes" regulate the rhythm through positive and negative "transcription-translation

feedback loops" (TTFLs).² The negative TTFL in mammals consists of the activators CLOCK and BMAL1, which bind to the E-boxes to activate transcription of repressor proteins Period (encoded by PER1/2/3) and Cryptochrome (CRY1/2).³ PER and CRY proteins heterodimerize and translocate back to the nucleus, repressing their own transcription by removing the CLOCK-BMAL1 complex.⁴ The consecutive events in TTFL, including transcription, mRNA processing, and translation, occur in a circadian fashion, to maintain the exact 24-h periodicity for many genes. However, major questions regarding how these rhythmic processes are spatiotemporally orchestrated remain unanswered.

In eukaryotic cells, complex biochemical reactions are delicately compartmentalized in order to facilitate precise



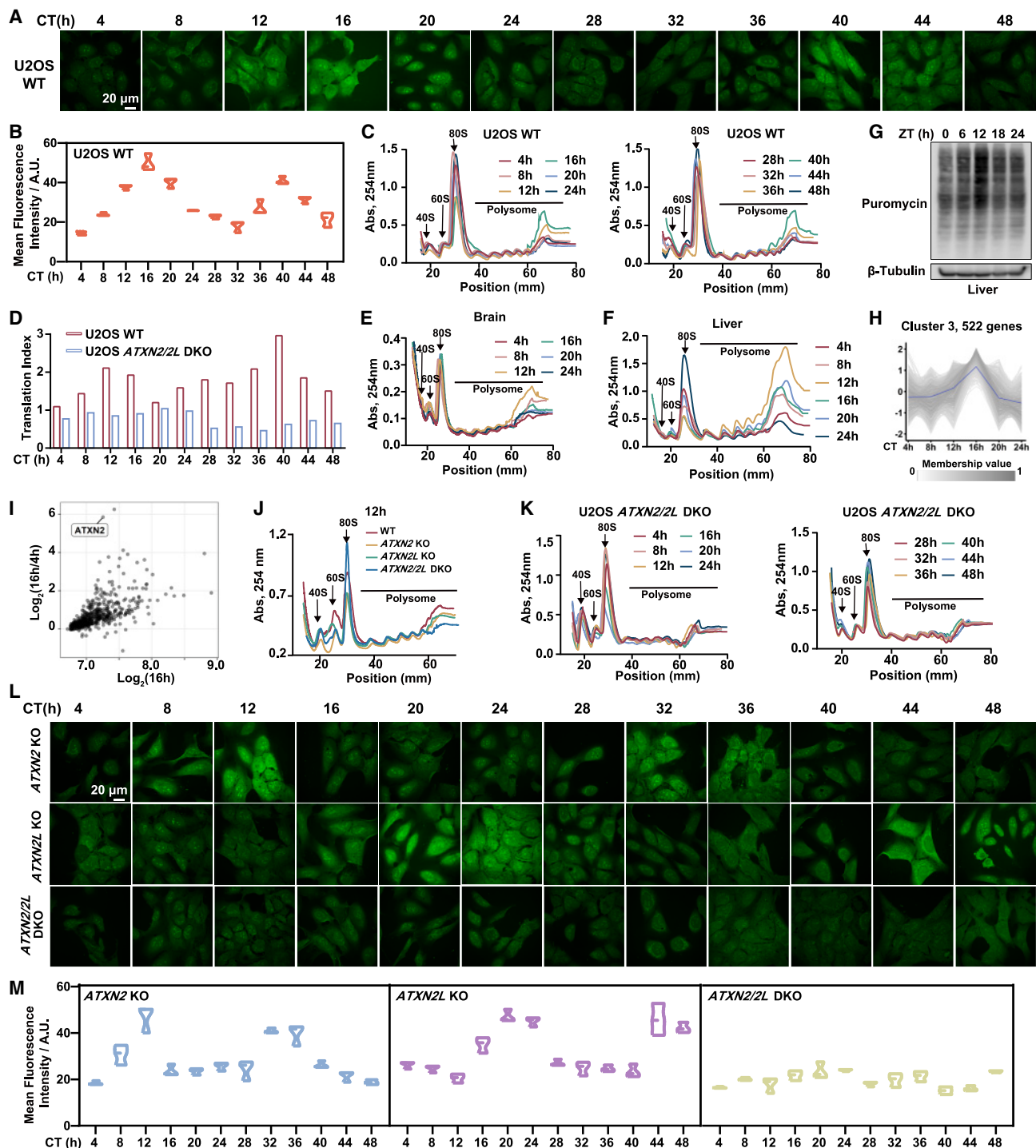


Figure 1. Protein synthesis oscillates along the circadian cycle and is regulated by ATXN2 and ATXN2L

(A) HPG fluorescent staining results showing protein synthesis activity at designated time points. U2OS cells were synchronized and pulse-labeled with HPG for 30 min, fixed, and subjected to Click-iT HPG reaction using the Alexa-fluor 488-azide capture agent. Scale bars, 20 μ m.

(B) Corresponding quantitative analysis of mean HPG fluorescence intensity in (A). Values represented means \pm SD ($n = 4$).

(C) Polysome profiles of U2OS cells collected at 4-h intervals for 48 h after synchronization. The peaks corresponding to 40S, 60S, and 80S were indicated by arrows, and polysome was marked on top.

(D) Quantitation of polysome fraction profile with translation index in (C) and (K).

(E and F) Polysome profiles of mouse brain (E) and liver (F) tissues collected at zeitgeber time (ZT) 4, 8, 12, 16, 20, and 24 h.

(legend continued on next page)

spatiotemporal control. Such compartmentalization can be achieved by canonical membrane-bound organelles such as mitochondria and endoplasmic reticulum, as well as via membrane-less organelles (MLOs).^{5,6} The MLOs are phase-separated dense macromolecular assemblies that mediate a plethora of subcellular processes, by enriching specific biomolecules and excluding others.

Here, we uncover the role of phase separation mediated by ATXN2 and ATXN2L in regulating oscillating translation in circadian rhythm. As an RNA-binding protein (RBP), ATXN2 is a well-established multi-functional regulator of post-transcriptional processes.^{7–9} In this study, we show that the ATXN2 and ATXN2L phase-separated condensates are spatiotemporally coordinated to rhythmically recruit translational machinery and specified groups of mRNA transcripts, allowing selective and temporal translational activation of the core circadian clock genes, which thereby serve as master regulators of rhythmic translation in mammals.

RESULTS

Protein synthesis oscillates along the circadian cycle and is regulated by ATXN2 and ATXN2L

We first focused on the rhythms of protein translation. Rhythmic protein synthesis was analyzed using the human bone osteosarcoma epithelial cell line U2OS, which is widely used in circadian studies.¹⁰ To this end, we treated U2OS cells with dexamethasone (DXMS), a strong inducer of robust circadian rhythms that resets and synchronizes the clock in cultured cells, typical for *in vitro* circadian entrainment,¹¹ and labeled newly synthesized proteins with noncanonical methionine analogs homopropargyl-glycine (HPG), which is visualized by azide-containing fluorescent dyes through copper-catalyzed cycloaddition (CLICK) reaction. We found that wild-type (WT) U2OS cells exhibited clear circadian rhythms of translational activation over 48 h (Figures 1A and 1B), which started to increase at 4 h or 28 h post initiation of circadian rhythm (CT4 or CT28), peaked at CT12–16 (and accordingly CT36–40), and swiftly decreased subsequently. Such translational oscillations ubiquitously exist in different cell types, such as THLE-2 and SH-SY5Y (Figures S1A and S1B).

Next, we performed polysome fractionation analysis as an alternative method to assess the global translation activity along the circadian cycle. Specifically, the ratio of areas under curves of heavy polysome (5+ ribosomes) and light polysome (2–4 ribosomes) was defined as the “translation index” (Figure S1C). This analysis showed that the translation index in WT U2OS cells was

low at CT4, peaked around CT12–CT16, followed by a decline at CT20–CT24. A similarly oscillating pattern was observed in the second circadian cycle as well (Figures 1C and 1D). Additionally, we employed a surface sensing of translation (SUnSET) technique to measure protein synthesis and detected rhythmic protein synthesis in corresponding cell lines (Figure S1D).

Oscillation of protein synthesis at the tissue level has been reported.¹² Consistently, we observed similar oscillation patterns in the brain and liver tissues (Figures 1E, 1F, S1E, and S1F), with a higher translation index observed at ZT12. Following injection of puromycin into the lateral ventricle (Lv), we observed rhythmic translational activation in the brain (Figure S1G). To assess the levels of newly synthesized proteins in the liver, we injected puromycin intraperitoneally and then performed western blot analysis with whole-tissue lysates (Figure 1G). Together, these results showed that active translational oscillation occurred in these two tissues.

We next set out to identify potential regulators of such rhythmic translation. To this end, we performed proteomic analyses with U2OS cells at six circadian time points. Via the fuzzy c-means clustering method, the proteins were then clustered into 7 different groups based on their temporal expressing patterns (Figures 1H and S1H). Interestingly, the proteins in cluster 3 (522 in total) exhibited a profile in high accordance with the translational activation pattern along circadian clocks (Figures 1A–1D and 1H).

Assuming that oscillatory RBPs were involved in the rhythmic activation of protein translation, we next calculated the fold changes of all cluster 3 proteins by comparing their peak levels at CT16 with the baseline levels at CT4 (Figure 1I). Interestingly, two RBPs were among the top 10 proteins with the highest increase from CT4 to CT16. One of the RBPs was ATXN2, which was ranked second in our analysis. The other RBP was DHX40, which is known to be primarily located in the nucleus.

To better understand the role of ATXN2 in rhythmic translational oscillation, we generated an ATXN2 KO U2OS cell line to explore the potential functions of ATXN2 in circadian regulation. Knockout (KO) of ATXN2 in U2OS cells resulted in a moderate reduction of the heavy polysome fractions at CT12, indicating that the overall rate of translation slightly decreased. We performed a bioinformatics analysis for ATXN2 and identified a paralog called ATXN2-like (ATXN2L), which shared high domain similarity with ATXN2 (Figure S1J). From an evolutionary aspect, the neighbor-joining tree for the orthologs of ATXN2 and ATXN2L indicated that ATXN2 and ATXN2L were rooted in common ancestors, pbp1 in yeast and atx-2 in insects (Figure S1K). Similar to ATXN2 KO, ATXN2L KO causes a modest decline in

(G) Representative immunoblot of newly synthesized polypeptide labeled by puromycin in mouse liver tissues at different zeitgeber times.

(H) Expression pattern of the proteins in cluster 3, detected by MS at different time points. Seven groups of genes were clustered according to their distinct temporal expressing patterns using the fuzz c-means clustering algorithm. Cluster 3 was shown here, and others were shown in Figure S1H. Blue lines indicated the analog curve of each cluster. The y axis represented the normalized protein abundance.

(I) Scatterplot showing the protein level changes at CT16 compared with CT4. The y axis showed the \log_2 fold changes of CT16 over CT4, and the x axis represented the \log_2 protein abundance at 16 h.

(J) Polysome profiles of cell lysate from WT (red), ATXN2 KO (yellow), ATXN2L KO (green), and ATXN2/2L DKO (blue) at CT12.

(K) Polysome profiles of ATXN2/2L DKO cells collected for 48 h. Corresponding quantitative analysis of translation index was indicated in (D).

(L) Representative images showing nascent protein synthesis at different time points using the Click-iT HPG Alexa-fluor 488 protein synthesis assay in ATXN2 KO, ATXN2L KO, and ATXN2/2L DKO U2OS cells.

(M) Corresponding quantitative analysis of mean HPG fluorescence intensity in (L). Values represented means \pm SD ($n = 4$).

translation index at CT12. Additionally, in ATXN2/2L double-KO (DKO) cells, the translation index fell significantly lower at CT12 (Figures 1J and S1I).

As indicated by the changes of translation index, the translational activation rhythm was almost completely disrupted upon KO of both ATXN2 and ATXN2L (Figures 1K and 1D). The HPG labeling assays also confirmed that the rhythm was lost in our DKO cells (Figures 1L and 1M). Interestingly, compared with the advanced phase shift in the ATXN2 KO cells, the ATXN2L KO cells exhibited a delayed phase shift, indicating a potential role of these two proteins in adjusting phases of circadian rhythm. Together, these results clearly demonstrated that ATXN2/2L together regulate the oscillated translational activation along the circadian rhythm.

ATXN2/2L constitute master regulators of translation in circadian rhythm

To assess the translation landscapes for individual genes at a genome-wide scale, we next performed ribosome profiling (Ribo-seq) at different circadian times and upon KO of ATXN2 or ATXN2L. Given the global shift of the translation efficiencies as shown in Figure 1, we normalized the counts of the ribosome-protected fragments (RPFs, i.e., ribosome footprints) from regular genes against the ribosome footprints of mitochondrial genes,^{13,14} as their translation machinery was distinct from and independent of the cytoplasmic translation system.

As shown in Figure 2A, the ribosome footprints exhibited a visible global increase at CT12 relative to CT4, which correlated well with our results shown in Figures 1A–1E. This pattern of translational activation appeared to be preserved in the ATXN2 or ATXN2L single-KO cell, not, however, in ATXN2/2L DKO cells (Figures 2B–2D). More specifically, we found that 8 out of 10 genes involved in the core process of circadian clocks were subjected to upregulation of their translation efficiencies, which were quantified as ratios of the RPF read counts to the RNA-seq read counts, at CT12 compared with CT4 in WT U2OS cell. Such a rhythmic translation activation pattern was largely abolished in ATXN2/2L DKO cells (Figure 2E).

Next, via gene ontology (GO) functional enrichment analysis, we found the genes characterized by upregulated translation efficiencies, i.e., genes with increased RPF and stable RNA reads at CT12 compared with CT4, were significantly enriched in the processes of RNA processing, splicing, and ribosome biogenesis (Figure 2F), which was consistent with the elevated general translation we observed at CT12. While the protein components of the ribosome and the translation initiation factors exhibited significantly upregulated translation efficiencies at CT12 compared with CT4 in the WT and single KO cells (Figures 2G and 2H), no such trend was observed in the DKO cells.

Indeed, we found no evidence for global translation repression in either of our single KO cells (Figures S2A and S2B), even though the activated translation landscape at CT12 was largely repressed in our DKO cells (Figure 2I). Seven out of the ten core circadian clock genes were repressed at the level of translation in our DKO cells (Figure 2J). More specifically, the set of genes exhibiting translational downregulation upon ATXN2/2L DKO significantly overlapped with genes translationally activated at CT12 of WT U2OS cells (Figure 2K). In further confirmation

of these results, most of the ribosomal proteins and the translation initiation factors were repressed at the level of translation in the ATXN2/2L DKO cells at CT12 (Figures 2L and 2M).

To clarify whether ATXN2/2L deletion also negatively affected transcriptional events upstream of translation, we measured the changes of RNA of the above clock genes, several ribosome component genes as well as translation initiation factors over 48 h. We found that their transcription oscillation was minimally affected by ATXN2/2L deficiency (Figure S2C), suggesting that ATXN2/2L primarily regulates translation.

To ensure that our results represented rhythm along circadian cycle, not affected by cell cycles or other factors, we assessed whether depletion of ATXN2/2L affected the overall fitness of the cells by monitoring their apoptosis and proliferation rates. To this end, we synchronized WT and ATXN2/2L single- and DKO cells and analyzed their viability by flow cytometry. The cell fraction of apoptotic cells differed little for the four cells at different time points (Figures S2D and S2E). In addition, cell proliferation rates were comparable (Figure S2F), indicating that despite impaired circadian translation, the ATXN2/2L KO cells were viable, with no abnormal cell death.

Together, these results showed that translation landscape oscillates along the circadian cycle, a process abolished in the absence of ATXN2 and ATXN2L.

ATXN2/2L puncta oscillate in sync with the circadian cycle

In order to investigate the mechanism underlying such rhythmic translation, we next examined the expression and distribution of Atxn2 and Atxn2l at different time points, by immunostaining of mouse tissues. We found that Atxn2 and Atxn2l were significantly enriched in the SCN (Figure S3A). Interestingly, both proteins appeared to form perinuclear puncta in the SCN (Figure 3A). We observed similar puncta in other brain regions such as the cortex, hippocampus, and cerebellum (Figure S3B). Transmission electron microscopy (TEM) analysis of white adipose tissue (WAT) and liver also revealed that Atxn2 and Atxn2l form cytoplasmic clusters (Figures 3B and 3C).

As ATXN2/2L proteins form puncta at specific intra-cellular locations, suggesting that phase separation is involved in their regulation. To test this assumption, we set out to identify drivers of ATXN2 and 2L phase separation by performing *in vitro* phase separation experiments. Both ATXN2 and ATXN2L contain multiple domains, including LSM (like-SM) and LSM-associated domains for RNA-binding, a PABP-associating motif (PAM2), and a long stretch of low-complexity domain (LCD) in the C terminus. The LCDs of both proteins were conserved among their orthologs in more than 200 species (Figures S3C and S3D).

ATXN2 LCD and ATXN2L LCD proteins both phase separated *in vitro* in a protein- and salt-concentration-dependent manner as expected (Figures 3D, 3E, S3E, and S3F). Fluorescence recovery after photobleaching (FRAP) results showed that fluorescence was bleached and recovered within a few minutes, suggesting the liquid property of ATXN2 and ATXN2L LCD droplets (Figure 3F).

To assess the subcellular localization of ATXN2/2L in more detail, we examined their presence in several cultured human cell lines, including a hypothalamic GnRH cell line GT1-7.¹⁵ We

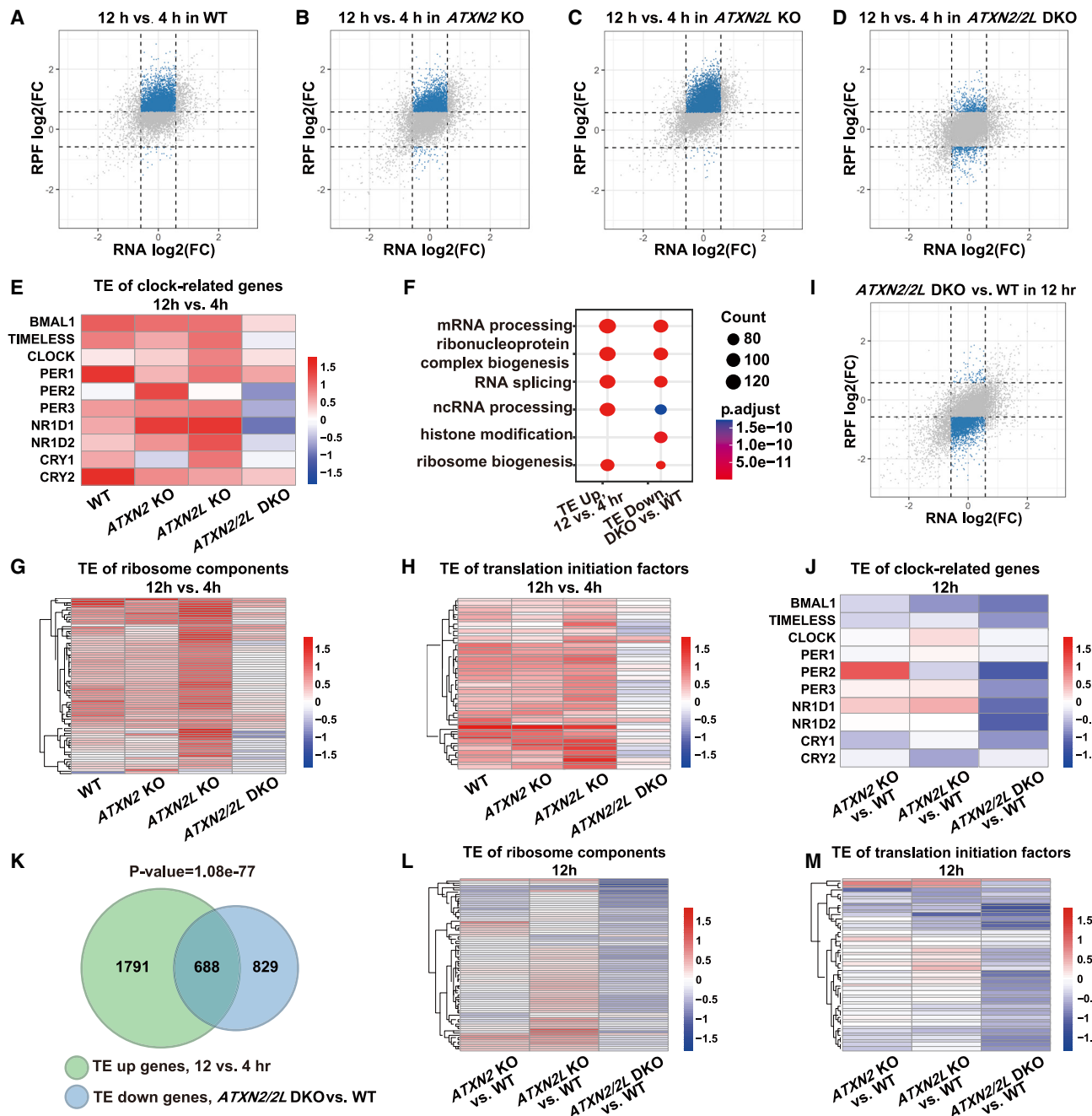


Figure 2. ATXN2/2L constitute master regulators of translation in circadian rhythm

(A–D and I) Scatterplots depicting the changes in translation-level (y axis) in response to transcriptome-level changes (x axis). The blue dots represent genes that are stable at the RNA level but exhibit changes in ribosome-protected footprint (RPF) levels. The threshold for log₂ (fold change) is set at 0.58. (A–D) showed the changes in WT, ATXN2 KO, ATXN2L KO, and DKO cells, respectively, between 12 h over 4 h. (I) showed the changes in DKO cells compared with WT cells at 12 h. (E, G, and H) Heatmap results showing the changes in translational efficiency (TE) of clock-related molecules (E), ribosome components (G) and translation initiation factors (H) in WT, ATXN2 KO, ATXN2L KO, and DKO cells, respectively, between 12 h over 4 h.

(F) Gene ontology analysis of TE upregulated genes of WT at CT12 over CT4 and TE downregulated genes of DKO cells against WT at CT12.

(J, L, and M) Heatmap results showing the changes in TE of clock-related molecules (J), ribosome components (L), and translation initiation factors (M) when comparing ATXN2 KO, ATXN2L KO, and DKO cells with WT cells at 12 h.

(K) TE upregulated genes of WT at 12 h over 4 h compared with TE downregulated genes of DKO cells against WT at 12 h. These two sets of genes overlapped significantly (p value = 1.09e-77, hypergeometric test).

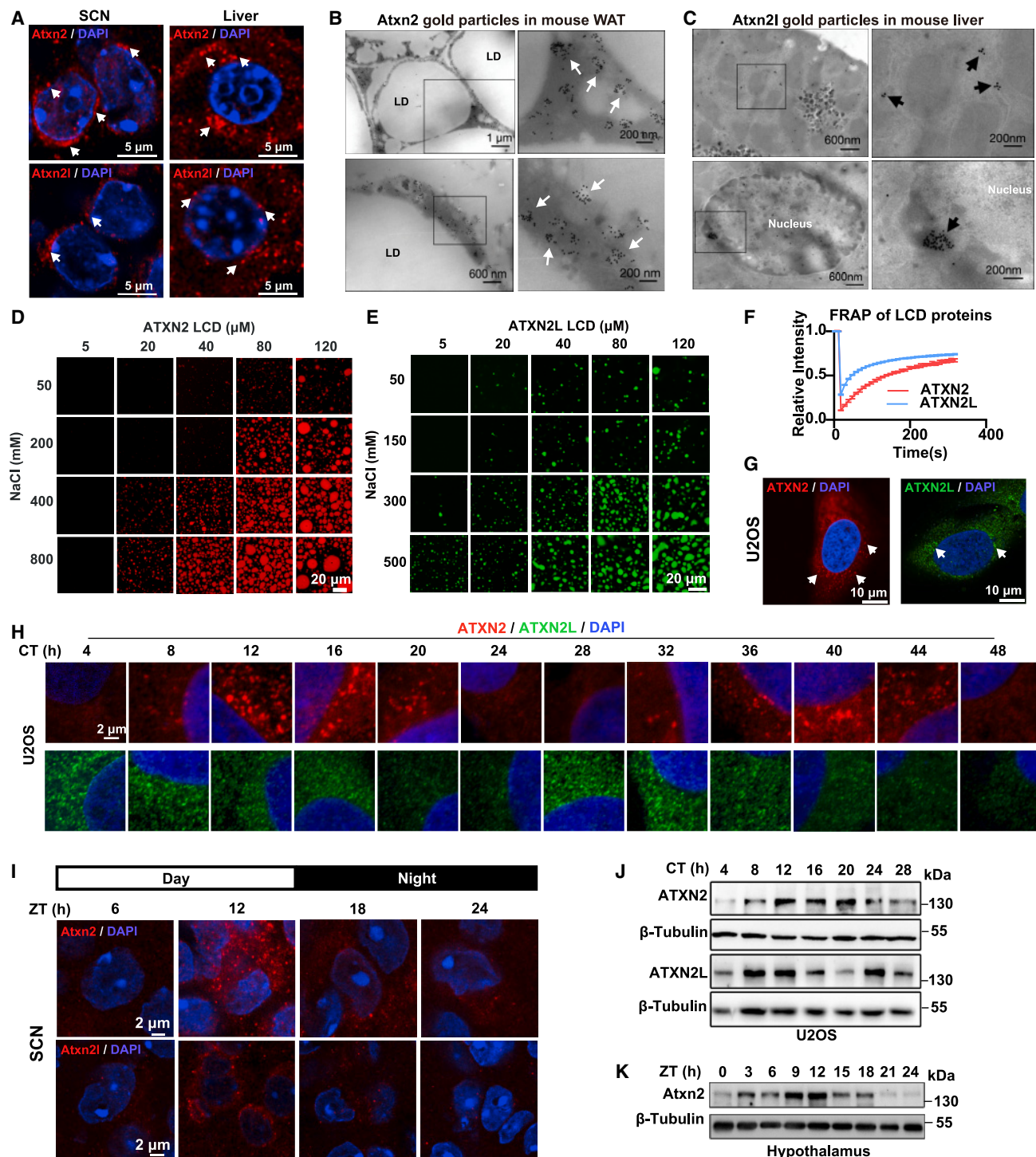


Figure 3. ATXN2/2L puncta oscillate in sync with the circadian cycle

(A) Representative immunofluorescence images illustrating the expression of Atxn2 or Atxn2l (red) in the SCN (left) and liver (right). The nucleus was labeled with DAPI (blue), and Atxn2 or Atxn2l puncta were marked with white arrows. Scale bars, 5 μm .

(B) Representative transmission electron microscopy (TEM) images of immunogold labeling of Atxn2 in the white adipose tissue (WAT) of mice. Lipid droplets were labeled as LD, and black dots represented Atxn2 proteins detected by gold particles. White arrows pointed to Atxn2 clusters. The scale bars were 1 μm , 600 nm, and 200 nm, respectively.

(C) Representative TEM images demonstrating the immunogold labeling of Atxn2l in mice. Black dots corresponded to Atxn2l proteins detected by 18 nm gold particles, and black arrows indicated Atxn2l clusters. The scale bars represent 600 and 200 nm, respectively.

(legend continued on next page)

detected prominent ATXN2/2L condensates by immunofluorescence in U2OS, THLE-2, GT1-7, and HeLa (Figures 3G and S3G). Co-staining with organelle markers showed that ATXN2 puncta were interdigitated with the endoplasmic reticulum (Figure S3H). The specificity of the antibody was validated in ATXN2 KO cell (Figure S3I).

Notably, we observed a high degree of heterogeneity in the number of the ATXN2 puncta within the cytoplasm, a fact that may be related to the heterogeneity of the cellular circadian clock. Remarkably, once cells were synchronized, the ATXN2/2L puncta oscillated in a time-dependent manner (Figure 3H), which peaked at CT12 to CT16 and markedly dropped afterward. We found that both the number and the size of ATXN2 puncta oscillated in sync with circadian cycle (Figures S3J–S3M). We observed similar rhythmicity for ATXN2 puncta in THLE-2 cells (Figures S3N and S3O) and further, in the SCN region, along a 24-h cycle (Figures S3I and S3P).

To dissect the mechanistic basis for the observed rhythmic oscillation of ATXN2/2L puncta, we examined their protein levels in several synchronized cell lines. ATXN2/2L protein levels exhibited rhythmic patterns, cycling over a period of 24 h (Figures 3J, S3Q, and S3R). Atxn2 protein levels also fluctuated rhythmically in our hypothalamus samples, where the central pacemaker SCN resides (Figures 3K and S3S), as well as in other brain regions (Figure S3T). ATXN2 mRNA levels in both U2OS cells and hypothalamus samples also exhibited a rhythmic pattern resembling a 24-h circadian cycle (Figures S3U and S3V).

Together, these results strongly suggest that the expression of both ATXN2 and 2L cycles over the circadian period, resulting in the fluctuation and cycling of the ATXN2/2L cellular puncta.

ATXN2 forms oscillatory translation initiation condensates

As the ATXN2 puncta oscillated in a circadian-cycle-dependent manner, we attempted to isolate ATXN2 condensates at different time points to analyze their components. We used a cryo-mill IP technique, which involved rapid immunoprecipitation at a close-to-native starting concentration that largely preserved the integrity of protein complexes and phase-separated condensates.^{16,17} We analyzed the proteins co-immunoprecipitated with ATXN2 at different time points using the RAIN (rhythmicity analysis incorporating nonparametric methods) algorithm¹⁸ and found that 52% of proteins displayed 24-h rhythms in lysates, which rose up to 70% in the group of ATXN2-associated proteins (Figure S4A), suggesting that ATXN2 condensates enrich cycling proteins.

We then defined different oscillating phase diagram anticipated by the RAIN algorithm to classify each protein into groups

that peaked at different time points (Figure S4B). ATXN2 condensates significantly enriched cycling proteins at its own expression peak (CT8–CT16), while these proteins distributed evenly in the cell lysates (Figure 4A), indicating the specific recruitment of these proteins in ATXN2 condensates. GO analysis of the immunoprecipitated proteins showed strong enrichments of mRNA processing and translation (Figure 4B). Moreover, proteins associated with mRNA processing or metabolism were specifically enriched at CT12, while translation-related proteins peaked from CT12 to CT16 (Figure 4C). These results suggested that ATXN2 condensates regulated different steps of mRNA-related events in a sequential manner.

To further analyze the putative function of the ATXN2-associated proteins at CT16, we performed network clustering analysis using a Markov clustering algorithm with the search tool for the retrieval of interacting genes/proteins program (STRING 9.1).¹⁹ One of the largest clusters of 25 proteins within the network, referred to as “translation-related proteins” cluster, included many well-characterized translation factors such as EIF2A, EIF3I, and ribosomal proteins (Figure 4D).

Further analysis showed that translation initiation factors and ribosomal proteins associated with ATXN2 cycled between CT12 and CT16, while such a pattern is absent in the cell lysates (Figures 4E and S4C). These events coincided with the spike of ATXN2 puncta, which was most conspicuous at CT12–CT16. Interestingly, the main translation initiation complex components, including EIF4G2, EIF4A4, EIF4B, EIF2A, and EIF2B, were enriched in ATXN2 condensates, in a cyclic manner with the highest peak at the CT12–CT16. The interactions between ATXN2 and corresponding translation-related proteins were confirmed by western blot (Figure 4F). In contrast to the observed enrichment of initiation complexes, we did not detect any translation elongation factors in the ATXN2 condensates.

Together, these results strongly suggested that ATXN2 condensates facilitate the assembly of the translation initiation complex by concentrating translation initiation complex and ribosomes. Indeed, the ribosome occupancy patterns along the coding sequence (CDS) of these genes keep consistent at different circadian time points or upon ATXN2/2L DKO (Figure S4D), suggesting that the ATXN2/2L-dependent rhythmic translation regulation are likely to take place during translation initiation.

ATXN2/2L condensates recruit translation machinery and specific mRNAs

Thus far, we have well demonstrated that ATXN2 and 2L positively regulate the translation in circadian rhythm and that they form oscillating puncta via phase separation. Next, we further

(D and E) Phase diagram of *in vitro* purified ATXN2 (D) or ATXN2L (E) LCD protein. The corresponding protein and NaCl concentrations were indicated. The Alexa-568 labeled ATXN2 LCD was shown in red, and the Alexa-488 labeled ATXN2L LCD was shown in green. Scale bars, 20 μm.

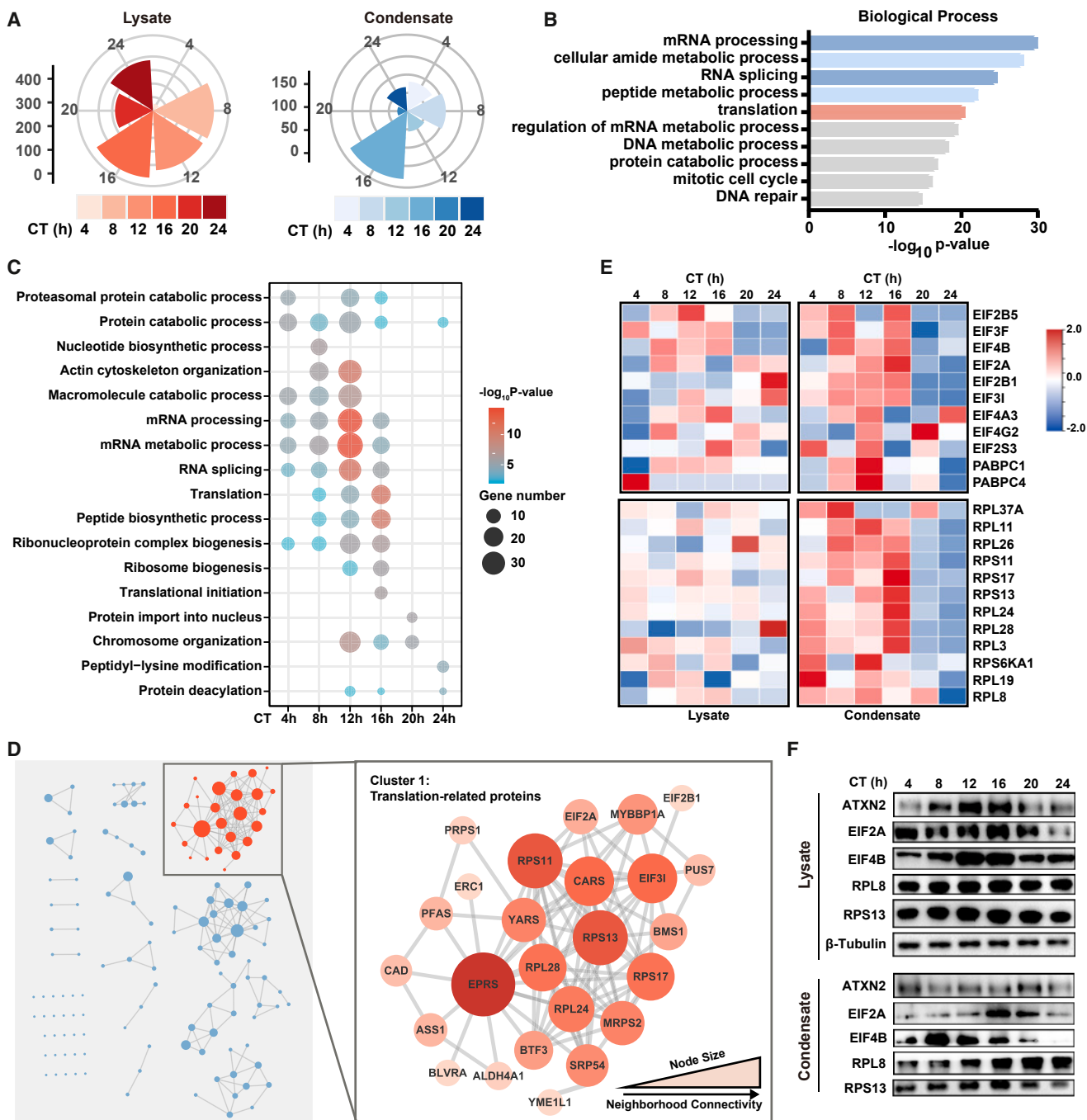
(F) FRAP curves for ATXN2 and ATXN2L liquid-like droplets. The values denoted means ± SD (n = 6).

(G) Representative immunofluorescence images showing the expression of ATXN2 (red) and ATXN2L (green) in U2OS cells. DAPI was shown in blue, and the white arrows pointed to ATXN2 or ATXN2L puncta. Scale bars, 10 μm.

(H) Representative images showing the expression of ATXN2 (red) and ATXN2L (green) in U2OS cells at different circadian time points. DAPI was shown in blue. Scale bars, 2 μm.

(I) Representative images showing the expression of Atxn2 and Atxn2l (red) in the SCNs at different zeitgeber times (ZTs). Scale bars, 2 μm.

(J and K) Western blot results showing the protein abundance of ATXN2 and ATXN2L in U2OS cells (J) and hypothalamus samples (K) at indicated time points along the circadian cycle. β-tubulin was used as a control.

**Figure 4. ATXN2 forms oscillatory translation initiation condensates**

- (A) Rose plot representing the phase distribution of cycling proteins in corresponding cell lysate and ATXN2 condensate groups. ATXN2 condensates groups indicated the immunoprecipitated proteins of ATXN2.
- (B) Gene ontology analysis of proteins enriched in ATXN2 condensates. The top 10 GO biological process annotations were shown in a bar chart ordered from the most frequent (top) to the least frequent (bottom), with the horizontal axis indicating the $-\log_{10}$ p value corresponding to each term.
- (C) Bubble plot showing the top terms in the GO biological process annotations for proteins enriched in ATXN2 condensates at different time points. The size of the dots represented the number of proteins enriched in the term, and the color of the dot represented the $-\log_{10}$ p value corresponding to each term.
- (D) ATXN2 interaction network demonstrated in clusters. Among them, the largest cluster contained 25 translation-related proteins, with node size indicating the connectivity degree.
- (E) Heatmap showing the enrichment of translation initiation factors (top) and ribosomal components (bottom) in ATXN2 condensates at different time points.
- (F) Western blot of ATXN2 co-immunoprecipitated proteins at different time points as shown above.

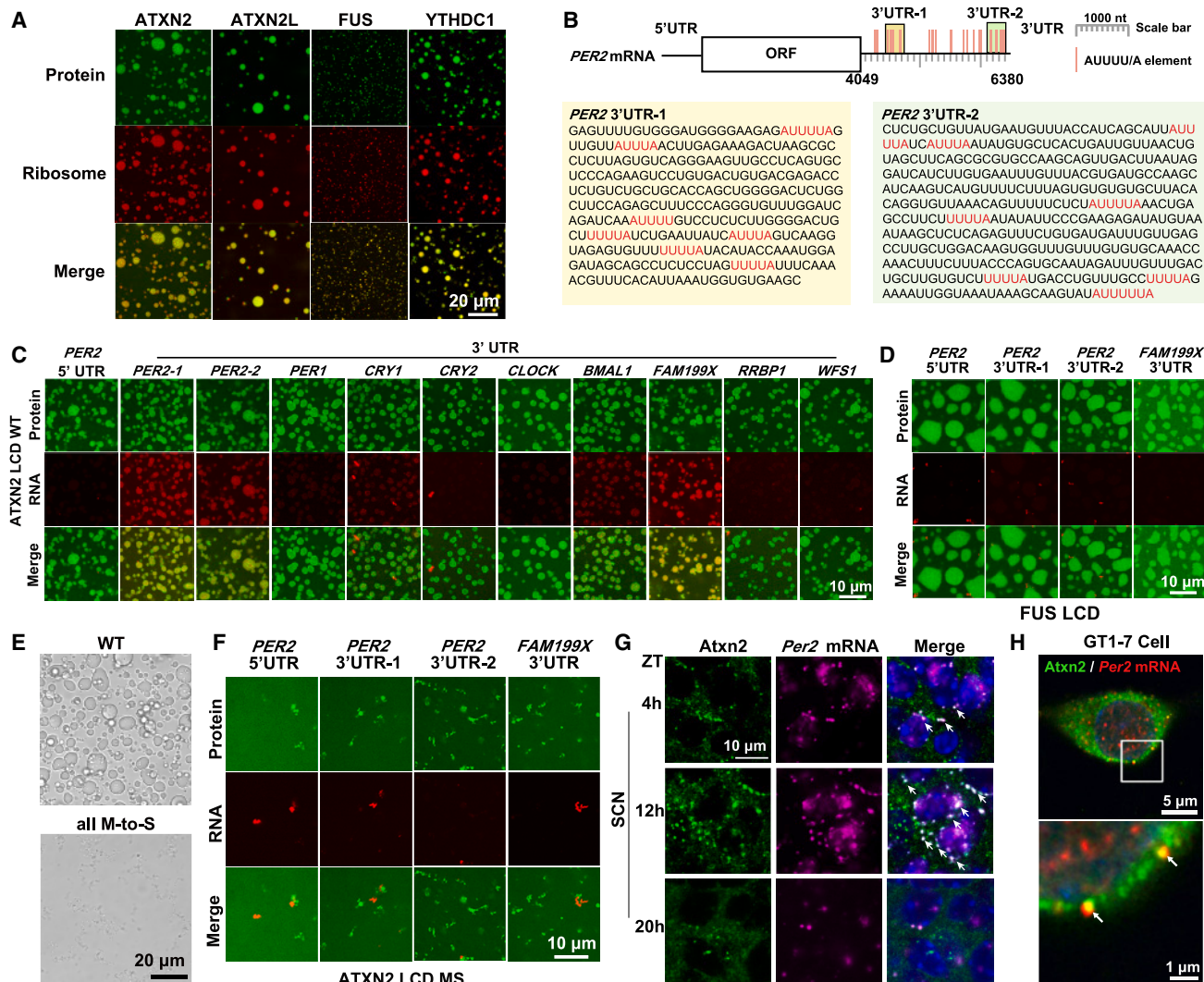


Figure 5. ATXN2/2L condensates recruit translation machinery and specific mRNAs

- (A) Multiple phase-separated condensates recruit ribosomes *in vitro*. The phase-separated liquid-like droplets formed by the LCDs of ATXN2, ATXN2L, FUS, and YTHDC1 were labeled in green. Purified ribosomes were labeled in red. Scale bars, 20 μ m.
- (B) Schematic diagram of the PER2 mRNA molecule, with the two AUUUU/A-rich sequences in the 3' UTR highlighted in yellow and light green, respectively. The AUUUU/A motifs were colored in red.
- (C) ATXN2 condensates selectively recruited specific RNAs *in vitro*. The ATXN2 LCD protein was colored in green, and RNAs including the PER2 5' UTR, two AUUUU/A-rich sub-regions of the PER2 3' UTR, PER1 3' UTR, CRY1 3' UTR, CRY2 3' UTR, CLOCK 3' UTR, BMAL1 3' UTR, FAM199X 3' UTR, RRBP1 3' UTR, and WFS1 3' UTR were shown in red. Scale bars, 10 μ m.
- (D and F) The FUS LCD (D) and ATXN2 all M-to-S mutant (F) failed to recruit specific RNAs *in vitro*. The proteins were colored in green, and RNAs were shown in red. Scale bars, 10 μ m.
- (E) Representative images showed the *in vitro* phase separation state of ATXN2 LCD wild-type and all M-to-S mutant. Scale bars, 20 μ m.
- (G) Representative images showing the co-localization of Per2 mRNA and Atxn2 protein condensates in SCN at different zeitgeber times. Immunostaining of Atxn2 protein was shown in green, Per2 mRNAs were shown in purple, and nuclei were labeled with DAPI (blue). The white arrows indicated the co-localized Atxn2 puncta and Per2 mRNAs. Scale bars, 10 μ m.
- (H) Representative images showing the co-localization of Per2 mRNA and Atxn2 protein condensates in hypothalamic GT1-7 cells. Immunostaining of Atxn2 protein was shown in green, Per2 mRNAs were shown in red, and nuclei were labeled with DAPI (blue). The white arrows indicated the co-localized Atxn2 puncta and Per2 mRNAs. Scale bars represent 5 and 1 μ m, respectively.

assessed how phase separation assisted in selectively recruiting translation machinery. We isolated the 80S ribosomal subunits and incubated them with ATXN2 and ATXN2L liquid-like droplets, which resulted in the enrichment of the ribosome complex

in vitro (Figure S5A). Other phase-separating systems, including those of FUS and YTHDC1, were used as controls. Our results showed that the ribosomes were enriched in phase-separated condensates with little selectivity (Figures 5A and S5B).

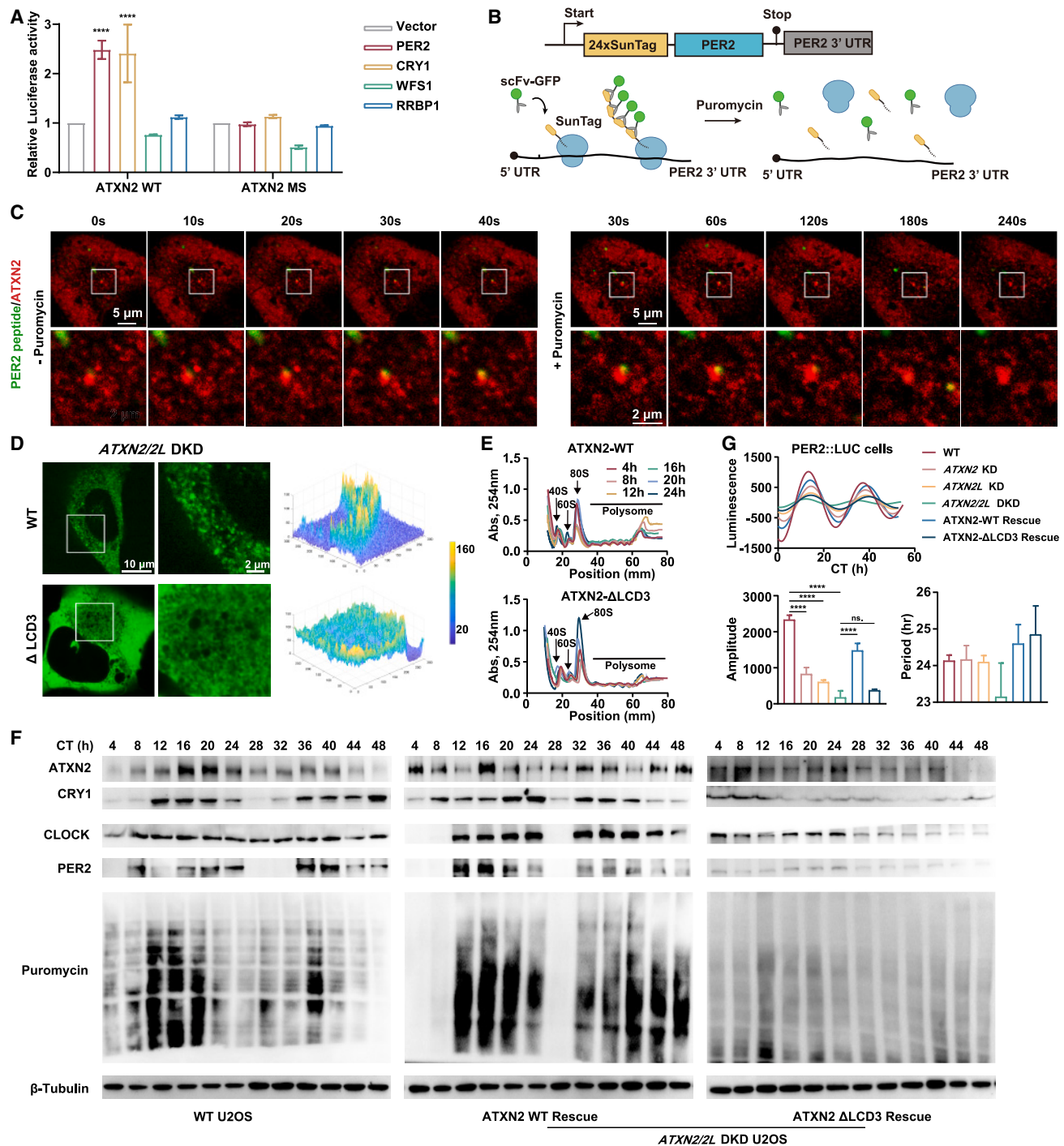


Figure 6. ATXN2/2L condensates activate PER2 translation *in vitro* and *in vivo*

(A) A histogram showing the *in vitro* translation efficiency with the addition of phase-separated ATXN2 LCD WT (ATXN2 WT, left) or all M-to-S mutant (ATXN2 MS, right) proteins, represented by the relative luciferase activity. Relative luciferase activities were quantified, from the expression of three constructs, luciferase control (gray), luciferase-PER2 3' UTR (red), luciferase-CRY1 3' UTR (yellow), luciferase-WFS1 3' UTR (green), or luciferase-RRBP1 3' UTR (blue), respectively. The relative luciferase activities were normalized by the luciferase of the control group. Values were shown as mean \pm SD ($n = 3$, *** $p < 0.00005$ by *t* test).

(B) Schematic diagram showing nascent polypeptide labeled with SunTag system and protein synthesis complex dissociated by addition of puromycin.

(C) Representative images of U2OS cells co-expressing scFv-GFP, the translation reporter (SunTag_{24x}-PER2-3'UTR) and mCherry-ATXN2 without (left) or with (right) puromycin-induced translational inhibition. The co-localization of nascent synthesized PER2 peptide (green), and mCherry-tagged ATXN2 protein (red) was indicated by the white box. Scale bars, 5 and 2 μ m, respectively.

(legend continued on next page)

We next assessed whether ATXN2/2L condensates selectively recruit mRNAs. A previous study based on PAR-CLIP experiments reported that ATXN2 predominantly binds to uridine-rich elements in mRNA, and more specifically to the AUUUU/A-rich motif.²⁰ We thus examined the sequence of a selection of core clock genes. We found that both *PER2* and *CRY1* mRNA harbor two long stretches of sequences rich in the AUUUU/A sequence in their 3' UTRs, but few in their 5' UTRs (Figures 5B and S5C).

Therefore, we *in vitro* transcribed eleven pieces of RNAs, *PER2* 5' UTR, two stretches of AUUUU/A-rich 3' UTR of *PER2*, the 3' UTR of several other clock genes, as well as *FAM199X*, a known ATXN2 substrate as a positive control, and two negative controls, *RRBP1* and *WFS1*, which did not bind ATXN2 and showed no rhythmic translation fluctuation according to Ribo-seq data. As shown in Figures 5C and S5E, *PER2* 3' UTRs were abundantly enriched in ATXN2 condensates; however, 5' UTRs lacked any enrichment. As expected, the two negative controls failed to be recruited to the ATXN2 droplets. Another two clock-related molecules, *CRY1* and *BMAL1*, were also recruited into the liquid-like droplets, strongly suggesting that selectivity is achieved via the 3' UTRs of the circadian clock genes.

To ensure that the observed binding was not related to unbiased retainment of the droplets, we used FUS droplets as a negative control. None of these RNAs were enriched by FUS droplets (Figure 5D). We also generated a series of control mutants that were deficient in their phase separation ability. As the methionine residues in Pbp1 (yeast atx2) drive phase separation,²¹ we generated single and all M-to-S mutants and tested their phase separation capacity (Figure S5F). M1268S single mutant and all M-to-S mutants no longer underwent phase separation (Figures 5E and S5G). When ATXN2 all M-to-S mutants no longer phase separated, the RNAs and proteins no longer co-localized (Figure 5F).

Inspired by the *in vitro* observations above, we then further tested the selective enrichment of *PER2* 3' UTR by ATXN2 phase separation *in vivo*. We conducted immunofluorescence coupled with RNAscope single-molecule fluorescence *in situ* hybridization to detect the location of *Per2* mRNAs relative to Atxn2 condensates in the mouse brain. The results were particularly significant in the SCN, where abundant *Per2* mRNAs co-localized with Atxn2 puncta in a rhythmic manner with a peak at CT12 (Figure 5G), which was further verified in hypothalamic GT1-7 cells (Figure 5H). The co-localization was not as prominent in other brain regions, suggesting a specific role of Atxn2 in activating *Per2* translation in the SCN (Figure S5H).

Together, these results suggested that ATXN2 condensates are able to enrich ribosome complexes and specific mRNAs such as *PER2*, which may further contribute to translational activation as a function of the circadian rhythm.

ATXN2/2L condensates activate PER2 translation *in vitro* and *in vivo*

Given that the ATXN2 condensates enrich translation machinery, we next assessed whether phase separation was required for translational activation. We first performed *in vitro* translation assays with either phase-separating or phase separation-deficient ATXN2 LCD proteins (Figure S6A). While the translation efficiency of PER2 and CRY1 spiked to 2- to 3-fold higher than control in ATXN2 condensates, we observed no visible changes in translation efficiency in the presence of ATXN2 M-S mutant protein (Figure 6A). Moreover, ATXN2 droplets failed to promote the translation of the two negative controls, WFS1 and RRBP1. These results strongly suggested that the translation activity of PER2 and CRY1 can be regulated within ATXN2 LCD phase-separated condensates.

We next confirmed our findings for dynamic translation events. To this end, we performed single-molecule detection using the SunTag system.²² To ensure accurate capture of translation events, we used the Tet-on system alongside doxycycline inducible expression of PER2 peptides. We were able to eliminate background fluorescence interfering with the signal, and to capture the nascent PER2 peptides labeled with SunTag (Figure 6B). We observed nascent PER2 peptides emerge from mCherry-ATXN2 condensates after the addition of doxycycline (Figure 6C), and the SunTag fluorescence signals disappeared from the ATXN2 condensates upon addition of the translation inhibitor puromycin (Figures 6B and 6C). These results confirmed that active translation events occur in phase separation system.

To provide direct evidence supporting the contribution of ATXN2 phase separation for translational activation, we performed rescue experiments by expressing ATXN2 full-length protein or ATXN2 mutants with specific residues deleted or mutated (Figure S6B) in ATXN2/2L DKO cells. Among them, the cells with ATXN2 deleting C-terminal LCD3 (925–1,312) were with no cytoplasmic condensates (Figures 6D and S6C). We then used polysome profiling and SUSET to evaluate the overall translation oscillation in both WT and ATXN2-ΔLCD3 cell lines. As expected, WT ATXN2 obviously rescued the translation inhibition of our double-KO cells, while ATXN2-ΔLCD3 mutant failed to (Figures 6E, 6F, and S6D).

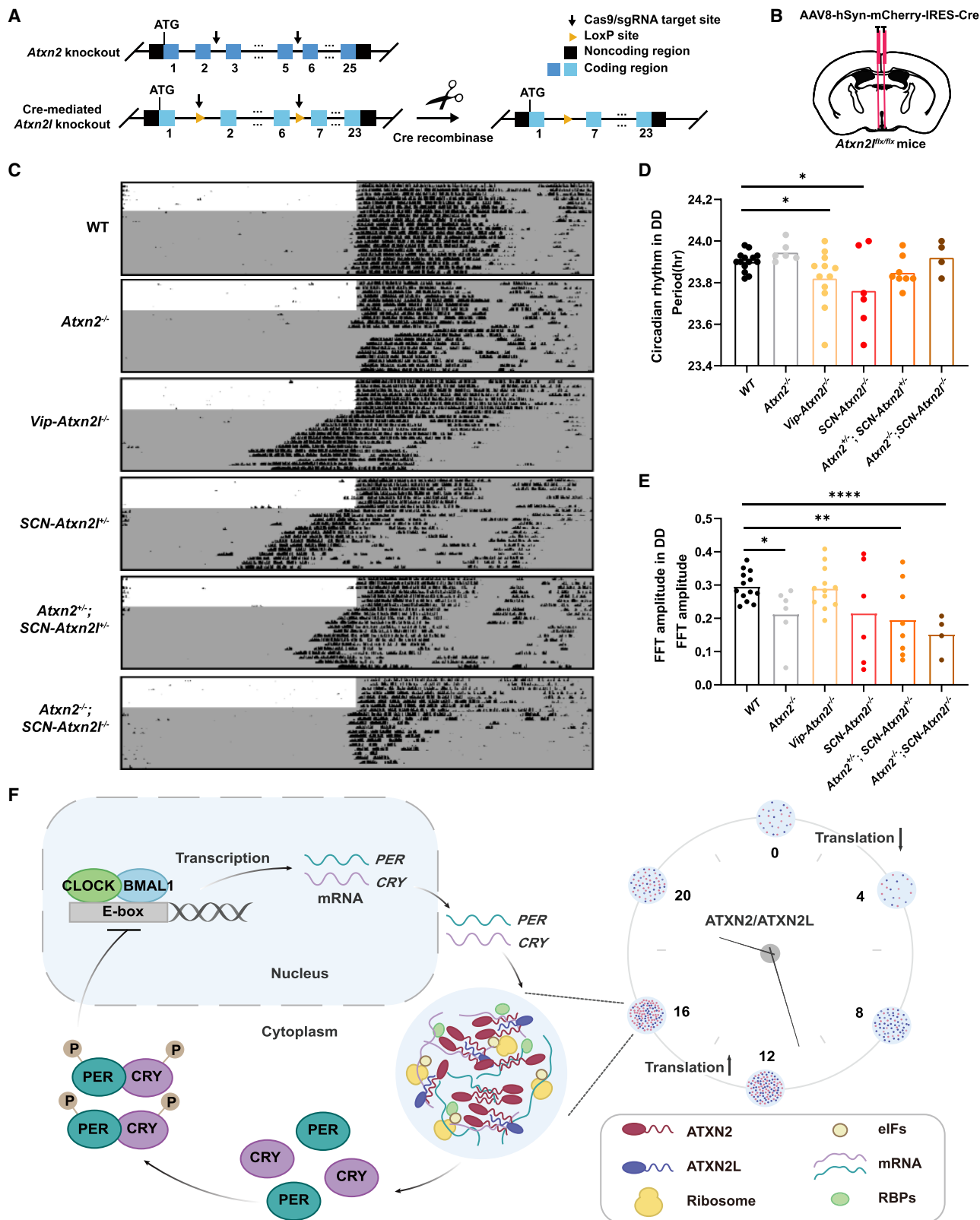
In addition, we tested whether the translation of core clock genes repressed upon DKO of ATXN2/2L could be rescued by ATXN2. CRY1, CLOCK, and PER2 protein showed an oscillated expression pattern in both WT and full-length ATXN2 rescue cells (Figure 6F). However, ATXN2-ΔLCD3 mutant was unable to promote the translation of these three clock proteins. In parallel, we measured cell-autonomous circadian-TTFL period and amplitude to determine whether phase separation of ATXN2 regulates the circadian behaviors of cultured cells. Using the PER2::LUC

(D) Representative images of EGFP-ATXN2 (top) and EGFP-ATXN2-ΔLCD3 (bottom) rescued in double-KO cells. A three-dimensional statistical graph of the gray value (right) was shown corresponding to the image. Scale bars, 10 and 2 μm, respectively.

(E) Polysome profiles of EGFP-ATXN2 (top) and EGFP-ATXN2-ΔLCD3 (bottom) rescued cells over 24 h. The peaks corresponding to 40S, 60S, 80S were indicated by arrows and polysome was marked on top.

(F) Western blot results showing the protein abundance of ATXN2, CRY1, CLOCK, PER2, and puromycin labeled nascent protein in wild-type U2OS cells (left), and EGFP-ATXN2 (middle) or EGFP-ATXN2-ΔLCD3 (right) rescued cells along a 48-h circadian cycle. β-tubulin was used as a control.

(G) Representative rhythms of PER2::LUC bioluminescence in ATXN2 KD, ATXN2L KD, ATXN2/2L DKD U2OS cells, as well as EGFP-ATXN2 and EGFP-ATXN2-ΔLCD3 rescued cells. Amplitude and period lengths of the bioluminescence rhythms were shown as mean ± SD (n = 3, ***p < 0.00005 by t test).



(legend on next page)

cell line previously reported,¹⁰ we measured luciferase reporter gene expression in ATXN2, ATXN2L single-, and double-knockdown (KD) cells by performing real-time luminometry experiments (Figure S6E). As shown in Figure 6G, circadian amplitude rhythms were defective in both ATXN2 and ATXN2L KD cells, but without changing the period length. ATXN2/2L double KD severely damped the high-amplitude phenotypes while slightly affected the circadian period length, suggesting the role of ATXN2/2L in sustaining the robustness of circadian rhythms. Interestingly, in ATXN2/2L DKO cells, WT ATXN2 rescued the abnormal cell-autonomous circadian behaviors, while the ATXN2-ΔLCD3 mutant failed, indicating that the phase separation of ATXN2 maintained both the 24-h periodicity and high-amplitude rhythms in cultured cells.

Together, these findings suggested that ATXN2 phase separation was required for the translational activation of PER2 and other clock molecules, as well as cell-autonomous circadian behaviors.

Atxn2 and Atxn2l together regulate the circadian rhythm in mice

To explore potential roles of Atxn2 and Atxn2l in physiological circadian regulation, we next generated several KO mouse strains. As the Atxn2l KO mouse is embryonically lethal,²³ we generated conditional tissue-specific KO mice, VIP-Cre-driver KO (*Vip-Atxn2l^{-/-}*), as well as SCN-AAV8-Cre-driver KO (*Atxn2l^{flox/flox}* mice injected with AAV8-mCherry-IRES-Cre in SCN are referred to as *SCN-Atxn2l^{-/-}*) (Figures 7A and 7B). Furthermore, we generated *Atxn2* and *Atxn2l* compound heterozygous (*Atxn2^{-/-}; SCN-Atxn2l^{+/-}*) and homozygous (*Atxn2^{-/-}; SCN-Atxn2l^{-/-}*) KO mice by injecting the AAV8-mCherry-IRES-Cre in the SCN of *Atxn2^{-/-}; Atxn2l^{flox/+}* mice and *Atxn2^{-/-}; Atxn2l^{flox/flox}* mice. mCherry-IRES-Cre expression in SCN was confirmed by fluorescence in brain sections (Figure S7A).

To monitor their circadian behavior, we continuously recorded the wheel-running activity of WT and genetically modified mice. Mice were initially maintained in a 12-h light/12-h dark cycle (LD) and subsequently shifted to constant darkness (DD). Four representative actograms of each mouse strain demonstrated their locomotor activities under both LD and DD (Figures 7C and S7B). All transgenic mice in LD conditions (Figure S7C), which were impacted by *Atxn2/2l* deficiency without exogenous zeitgebers,

did not exhibit any discernible changes in circadian behavior. Under DD, WT mice exhibited an average period of 23.90 ± 0.05 h (mean \pm SD, n = 14) calculated by χ^2 periodogram, while the stable period for *Atxn2^{-/-}* mutants slightly lengthened to 23.95 ± 0.05 h (n = 6, t test, p = 0.0655). In contrast, two types of *Atxn2l*-KO mice, (*Vip-Atxn2l^{-/-}*) and (*SCN-Atxn2l^{-/-}*), both exhibited significantly shortened period to 23.82 ± 0.13 and 23.76 ± 0.17 , respectively. However, the circadian period was not significantly affected in compound heterozygous or homozygous KO mice (Figure 7D).

Besides the shift in the period, we also measured other circadian-related parameters, such as the amplitude of the rhythm to indicate the robustness of the circadian rhythm.²⁴ As shown in Figure 7E, the results did significantly differ between WT (amplitude: 0.296 ± 0.044) and compound KO mice. Power spectral analysis using fast Fourier transform (FFT) detected lower-amplitude rhythm for compound heterozygous KO mice in DD (amplitude: 0.190 ± 0.106). More severe loss of circadian amplitude was observed in compound homozygous KO mice (amplitude: 0.153 ± 0.057).

Moreover, to ensure that the changes in periodicity and high-amplitude rhythms were not caused by physiological variations, we checked all transgenic mice for their weight, locomotor activity, and anxiety-like behavior. All of these parameters were normal (Figures S7D–S7H).

Together with our observations in KO cells, these results indicated that ATXN2 and 2L cooperate in regulating rhythmic translation to sustain circadian behaviors in mammals.

DISCUSSION

Circadian rhythm regulation requires exquisite coordination among multiple steps of transcription-translation and negative feedback. Here, we propose a model that the mammalian ATXN2 and ATXN2L form circadian-dependent condensates in mammals and regulate translation initiation of the central clock genes PER2 and CRY1. We have demonstrated *in vivo* and *in vitro* that ATXN2 and ATXN2L together regulate translation of PER2 and CRY1, the two major negative regulators in TTFL, and thereby mediate the circadian clock. At a specific period in the cycle, ATXN2 condensates sequentially enrich mRNA processing components and translation initiation machinery for

Figure 7. Atxn2 and Atxn2l together regulate the circadian rhythm in mice

- (A) Cartoon illustrating the strategy for knockout of *Atxn2* and *Atxn2l*. Exons are represented as numbered boxes, and Cas9/sgRNA target sites are depicted by black arrows. Yellow triangles indicate the two LoxP sites for *Atxn2l* conditional knockout mice.
- (B) *Atxn2l^{flox/flox}* mice were subjected to bilateral injections of AAV-hSyn-mCherry-IRES-Cre into the SCN and were allowed to recover for more than 2 weeks.
- (C) The representative single-plotted actograms of voluntary wheel-running activity in light-dark (LD) and dark-dark (DD) of WT, three types of single-knockout mice *Atxn2^{-/-}*, *Vip-Atxn2l^{-/-}*, *SCN-Atxn2l^{-/-}* and *Atxn2^{-/-}; SCN-Atxn2l^{-/-}* compound heterozygous knockout mice as well as *Atxn2^{-/-}; SCN-Atxn2l^{-/-}* compound homozygous knockout mice. Mice were housed in 12L:12D for 7 days, followed by a shift to constant darkness for 14 days. White shading indicates lights on, while gray shading represents lights off.
- (D) Average circadian free-running periods (mean \pm SD) were measured by chi-square periodogram in DD over 14 days from the same animals depicted in (C). The period for *Atxn2^{-/-}* mutants slightly lengthened to 23.95 ± 0.05 h (n = 6, p = 0.0655, t test). The length of period was significantly reduced in *Vip-Atxn2l^{-/-}* (n = 12, p = 0.0476, t test) and *SCN-Atxn2l^{-/-}* (n = 6, p = 0.0192, t test) mice.
- (E) Average amplitudes of locomotor activity rhythms were analyzed by fast Fourier transform (FFT) in DD over 14 days. The amplitude of *Atxn2^{-/-}* mice was significantly lowered to 0.213 ± 0.086 (n = 6, p = 0.011, t test). Compound heterozygous knockout mice (n = 8, p = 0.0089, t test) and compound homozygous knockout (n = 4, p < 0.0001, t test) mice showed a more severe loss of amplitude.
- (F) Schematic model illustrating that in the transcription-translation feedback loop, ATXN2 and ATXN2L form oscillating puncta along the circadian cycle, activating the translation of PER and CRY mRNAs through recruiting translation machinery components.

translational activation. Among the enriched translational components, the ATXN2 condensates specifically recruit mRNAs to achieve translational specificity (Figure 7F).

ATXN2 was previously known to be a risk factor in spinocerebellar ataxia-2²⁵ and ALS.²⁶ Its physiological function is diverse, including regulators of mRNA processing, stability, and expression.^{7,20} In *Drosophila*, Atx2 was reported to regulate circadian rhythm by assisting Per translation.²⁷ However, the changes in the circadian rhythm of *Atxn2* KO mammals appear to be subtle.²⁴ The evolutionary analysis provides two possible explanations. First, fly Atx2 interacts with Twenty-four (Tyf), a translational activator, and binds to *Period* (*per*) mRNA to initiate its translation. However, the Tyf protein is only found in Diptera insects, and is not conserved in mammals.²⁸ Second, ATXN2L first arose from a gene duplication event 500 million years ago, following the disappearance of Tyf. Our work strongly supports the importance of ATXN2L. Functional redundancy is commonly observed in the regulation of circadian rhythm, as evidenced by the multiple isoforms that exist for many clock proteins, for instance, Cry1 and Cry 2,²⁹ as well as mPer1-3.³⁰⁻³² This increased complexity suggests that mammals require far more sophisticated circadian regulation that allows for proper maintenance of all physiological functions of the entire organism.

Phase separation is frequently associated with cellular processes that undergo temporal variation, owing to its dynamic nature. Most of the previously described phase separation systems were investigated under cellular contexts at steady and homogenized states (e.g., stress conditions) or during unidirectional shifts (e.g., cell differentiation and development). Here, we show the physiological function of a flow of fluctuating phase separation system regulating cellular rhythm. Previous studies on transcriptional regulation have demonstrated the emergence of distinct condensates at various stages of the transcription process, which includes initiation, elongation, and termination.³³⁻³⁵ A liquid information flow model previously proposed to explain how transcription is achieved may also apply to the process of translation. Based on our own findings, we propose that translation is initiated in ATXN2 condensates, and other phase-separation-dependent or -independent machinery subsequently assists the protein translation to move into the elongation stage. Moreover, an uncoupling between circadian mRNA and protein was previously reported.³⁶ While our findings clearly show that ATXN2 phase-separated condensates play an essential role in translational activation, it might also be one of the underlying mechanisms for such uncoupling. In summary, our work allows a more detailed understanding of how phase separation performs spatiotemporal regulation of various cellular activities.

In addition, our work also has important implications for future disease studies. Recent experimental evidence suggests a bi-directional relationship between circadian rhythm disorders and a number of malignant human diseases, including tumors, type 2 diabetes, psychiatric disorders, and neurodegenerative diseases.³⁷ The onset of these diseases is insidious and progressive, with a disturbance of circadian rhythm observed at their early stages.³⁷ Sleep-related pathologies have been reported in SCA2 patients, including progressive loss of dream recall and reduction of REM density.³⁸ ATXN2 constitutes

a potent modifier of Tar-DNA binding protein (TDP-43) proteino-pathies.²⁶ ATXN2 antisense oligonucleotides (ASOs) have been suggested as an effective therapy for ALS.³⁹ Based on the rhythmicity of ATXN2 condensates unveiled in this study, the timing of diagnosis and therapeutic interventions should be carefully considered in future therapies.

It is worth noting that, while the core clock of mammals is regulated by interlocked positive and negative feedback loops, we primarily focused on resolving the role of ATXN2/2L in the negative TTFL. In addition to the first negative feedback loop, a second positive loop exists that involves Nr1d1/Reverb-alpha and RORs,^{2,40} as well as a tertiary TTFL involving Dec1/Dec2.⁴¹ The Rev-Erb α works in conjunction with Rev-Erb β and ROR α , together regulating the circadian expression of BMAL1. The oscillating expression of Nr1d1/Reverb-alpha and RORs is not only in the SCN but has also been proposed to coordinate the circadian metabolic process. Further, while our attention is directed toward the intrinsic cellular mechanisms, the mammalian circadian rhythm is susceptible to be entrained by external cues. Many SCN neurons are subject to light stimuli via the retina.⁴² Peripheral organs such as the liver are amenable to numerous input and output pathways, in conjugation with varying metabolic states.⁴³ Further investigations will be imperative for enhanced comprehension of the coordination between phase separation and circadian rhythm.

In conclusion, our findings shed light on the physiological relevance of the rhythmic ATXN2/2L-mediated phase separation and should greatly assist future studies of circadian regulation and the development of biomarkers for circadian rhythm disorders and related degenerative diseases.

Limitation of the study

Due to the limitation of the two conditional KO strategies for generating *Atxn2* KO mice, the behavioral alterations from *Atxn2*/KO might not be accurately represented. The VIP neuron represents only one-third of the SCN neurons, and the injection of AAV8-Cre-virus into SCN heavily depends on the diffusion and efficiency of the virus. The partial ablation of *Atxn2*/KO might account for the weak changes in mice behavior.

In addition, our knowledge of the ATXN2 recognized motif is based on previous PAR-CLIP results that identified “AUUUU/A” motif. However, additional motifs may confer such specificity of ATXN2. Further investigations should unveil more regulatory mechanisms underlying the selectivity of ATXN2 condensates.

STAR★METHODS

Detailed methods are provided in the online version of this paper and include the following:

- KEY RESOURCES TABLE
- RESOURCE AVAILABILITY
 - Lead contact
 - Materials availability
 - Data and code availability
- EXPERIMENTAL MODEL AND STUDY PARTICIPANT DETAILS
 - Cell lines

- CRISPR KO cell lines
- Mouse models
- **METHOD DETAILS**
 - Protein synthesis assay using Click-iT HPG system
 - Polysome profiling
 - Surface sensing of translation (SUnSET) assay
 - Phylogenetic tree construction
 - Ribosome profiling (Ribo-seq) library preparation and sequencing
 - RNA-seq and Ribo-seq data processing and analysis
 - Apoptosis assay by flow cytometry
 - Cell proliferation assay
 - Cell cycle analysis with flow cytometry
 - Quantitative real-time PCR
 - Immunofluorescence (IF)
 - Immunogold electron microscopy
 - Protein conservation analysis
 - Protein expression and purification
 - *In vitro* phase separation assays
 - Fluorescence recovery after photobleaching (FRAP) measurements
 - Western blot
 - Cryo-mill immunoprecipitation
 - Mass spectrometry data collection and analysis
 - Bioinformatic and statistical analyses of proteomics data
 - Cellular puncta analysis
 - Purification of human 80S ribosomal subunits
 - LLPS *in vitro* recruitment assays
 - RNA fluorescence *in situ* hybridization
 - Single-molecule fluorescent *in situ* hybridization in combination with immunocytochemistry
 - *In vitro* translation assay
 - SunTag and fluorescence imaging
 - Bioluminescence Recording
 - Lentiviral production
 - Adeno-associated viruses (AAV) packaging and stereotoxic surgery
 - Behavioral analysis of mouse locomotor activity rhythms
 - Open Field Test
- **QUANTIFICATION AND STATISTICAL ANALYSIS**

SUPPLEMENTAL INFORMATION

Supplemental information can be found online at <https://doi.org/10.1016/j.cell.2023.05.045>.

ACKNOWLEDGMENTS

The authors thank Drs. Songhai Shi, Li Yu, Pilong Li, E. Erquan Zhang, Maojun Yang, and other colleagues for discussions and valuable suggestions. We appreciate Drs. Yingqing Li, Xiaohua Shen, Weirui Ma, Yi Zhong, and E. Erquan Zhang for providing plasmids, cells, and mice. This work was supported by grants from the National Natural Science Foundation of China (32170684 to Y.L. and 81972912 to X.Y.) and the Ministry of Science and Technology of the People's Republic of China (2022ZD0213900 and 2022ZD0204900 to Y.L. and 2016YFC0906001 to X.Y.); and the facilities of Genome Sequencing and Analysis, and the facilities of Genome Sequencing and Analysis, and Bio-computing in the Tsinghua University Technology Center for Protein Research.

AUTHOR CONTRIBUTIONS

S.X. conducted mice behavior experiments. X.Y., Z.L., and C.S. performed the Ribo-seq and analyzed the data. B.L. conducted immunohistochemistry and RNA fluorescence *in situ* hybridization. Y.C. performed mass spectrometry experiment. The remaining experiments were performed or assisted by Y.Z.

DECLARATION OF INTERESTS

The authors declare no competing interests.

Received: December 12, 2022

Revised: April 12, 2023

Accepted: May 29, 2023

Published: June 26, 2023

REFERENCES

1. Hastings, M.H., Maywood, E.S., and Brancaccio, M. (2018). Generation of circadian rhythms in the suprachiasmatic nucleus. *Nat. Rev. Neurosci.* 19, 453–469.
2. Takahashi, J.S. (2017). Transcriptional architecture of the mammalian circadian clock. *Nat. Rev. Genet.* 18, 164–179.
3. Gekakis, N., Staknis, D., Nguyen, H.B., Davis, F.C., Wilsbacher, L.D., King, D.P., Takahashi, J.S., and Weitz, C.J. (1998). Role of the CLOCK protein in the mammalian circadian mechanism. *Science* 280, 1564–1569.
4. Kume, K., Zylka, M.J., Sriram, S., Shearman, L.P., Weaver, D.R., Jin, X., Maywood, E.S., Hastings, M.H., and Reppert, S.M. (1999). mCRY1 and mCRY2 are essential components of the negative limb of the circadian clock feedback loop. *Cell* 98, 193–205.
5. Banani, S.F., Lee, H.O., Hyman, A.A., and Rosen, M.K. (2017). Biomolecular condensates: organizers of cellular biochemistry. *Nat. Rev. Mol. Cell Biol.* 18, 285–298.
6. Bracha, D., Walls, M.T., and Brangwynne, C.P. (2019). Probing and engineering liquid-phase organelles. *Nat. Biotechnol.* 37, 1435–1445.
7. Inagaki, H., Hosoda, N., Tsuji, H., and Hoshino, S.I. (2020). Direct evidence that ataxin-2 is a translational activator mediating cytoplasmic polyadenylation. *J. Biol. Chem.* 295, 15810–15825.
8. Ostrowski, L.A., Hall, A.C., and Mekhail, K. (2017). Ataxin-2: from RNA control to human health and disease. *Genes (Basel)* 8, 157.
9. Singh, A., Hulsmeier, J., Kandi, A.R., Pothapragada, S.S., Hillebrand, J., Petruskas, A., Agrawal, K., Rt, K., Thiagarajan, D., Jayaprakashappa, D., et al. (2021). Antagonistic roles for ataxin-2 structured and disordered domains in RNP condensation. *eLife* 10, e60326.
10. Zhang, E.E., Liu, A.C., Hirota, T., Miraglia, L.J., Welch, G., Pongsawakul, P.Y., Liu, X., Atwood, A., Huss, J.W., 3rd, Janes, J., et al. (2009). A genome-wide RNAi screen for modifiers of the circadian clock in human cells. *Cell* 139, 199–210.
11. Balsalobre, A., Brown, S.A., Marcacci, L., Tronche, F., Kellendonk, C., Reichardt, H.M., Schütz, G., and Schibler, U. (2000). Resetting of circadian time in peripheral tissues by glucocorticoid signaling. *Science* 289, 2344–2347.
12. Janich, P., Arpat, A.B., Castelo-Szekely, V., Lopes, M., and Gatfield, D. (2015). Ribosome profiling reveals the rhythmic liver transcriptome and circadian clock regulation by upstream open reading frames. *Genome Res.* 25, 1848–1859.
13. Ingolia, N.T., Brar, G.A., Stern-Ginossar, N., Harris, M.S., Talhouarne, G.J., Jackson, S.E., Wills, M.R., and Weissman, J.S. (2014). Ribosome profiling reveals pervasive translation outside of annotated protein-coding genes. *Cell Rep.* 8, 1365–1379.
14. Iwasaki, S., Floor, S.N., and Ingolia, N.T. (2016). Rocaglates convert DEAD-box protein eIF4A into a sequence-selective translational repressor. *Nature* 534, 558–561.

15. Gillespie, J.M., Chan, B.P., Roy, D., Cai, F., and Belsham, D.D. (2003). Expression of circadian rhythm genes in gonadotropin-releasing hormone-secreting GT1-7 neurons. *Endocrinology* 144, 5285–5292.
16. Oeffinger, M., Wei, K.E., Rogers, R., DeGrasse, J.A., Chait, B.T., Aitchison, J.D., and Rout, M.P. (2007). Comprehensive analysis of diverse ribonucleoprotein complexes. *Nat. Methods* 4, 951–956.
17. Shi, Y., Pellarin, R., Fridy, P.C., Fernandez-Martinez, J., Thompson, M.K., Li, Y., Wang, Q.J., Sali, A., Rout, M.P., and Chait, B.T. (2015). A strategy for dissecting the architectures of native macromolecular assemblies. *Nat. Methods* 12, 1135–1138.
18. Thaben, P.F., and Westermark, P.O. (2014). Detecting rhythms in time series with RAIN. *J. Biol. Rhythms* 29, 391–400.
19. Brohee, S., and van Helden, J. (2006). Evaluation of clustering algorithms for protein-protein interaction networks. *BMC Bioinformatics* 7, 488.
20. Yokoshi, M., Li, Q., Yamamoto, M., Okada, H., Suzuki, Y., and Kawahara, Y. (2014). Direct binding of ataxin-2 to distinct elements in 3' UTRs promotes mRNA stability and protein expression. *Mol. Cell* 55, 186–198.
21. Yang, Y.S., Kato, M., Wu, X., Litsios, A., Sutter, B.M., Wang, Y., Hsu, C.H., Wood, N.E., Lemoff, A., Mirzaei, H., et al. (2019). Yeast ataxin-2 forms an intracellular condensate required for the inhibition of TORC1 signaling during respiratory growth. *Cell* 177, 697–710.e17.
22. Yan, X., Hoek, T.A., Vale, R.D., and Tanenbaum, M.E. (2016). Dynamics of translation of single mRNA molecules in vivo. *Cell* 165, 976–989.
23. Key, J., Harter, P.N., Sen, N.E., Gradhand, E., Auburger, G., and Gispert, S. (2020). Mid-Gestation lethality of Atxn2l-Ablated Mice. *Int. J. Mol. Sci.* 21, 5124.
24. Pfeffer, M., Gispert, S., Auburger, G., Wicht, H., and Korf, H.W. (2017). Impact of ataxin-2 knock out on circadian locomotor behavior and PER immunoreaction in the SCN of mice. *Chronobiol. Int.* 34, 129–137.
25. Pulst, S.M., Nechiporuk, A., Nechiporuk, T., Gispert, S., Chen, X.N., Lopes-Cendes, I., Pearlman, S., Starkman, S., Orozco-Diaz, G., Lunkes, A., et al. (1996). Moderate expansion of a normally biallelic trinucleotide repeat in spinocerebellar ataxia type 2. *Nat. Genet.* 14, 269–276.
26. Elden, A.C., Kim, H.J., Hart, M.P., Chen-Plotkin, A.S., Johnson, B.S., Fang, X., Armakola, M., Geser, F., Greene, R., Lu, M.M., et al. (2010). Ataxin-2 intermediate-length polyglutamine expansions are associated with increased risk for ALS. *Nature* 466, 1069–1075.
27. Lim, C., and Allada, R. (2013). Ataxin-2 activates PERIOD translation to sustain circadian rhythms in *Drosophila*. *Science* 340, 875–879.
28. Lim, C., Lee, J., Choi, C., Kilman, V.L., Kim, J., Park, S.M., Jang, S.K., Allada, R., and Choe, J. (2011). The novel gene twenty-four defines a critical translational step in the *Drosophila* clock. *Nature* 470, 399–403.
29. van der Horst, G.T., Muijtjens, M., Kobayashi, K., Takano, R., Kanno, S., Takao, M., de Wit, J., Verkerk, A., Eker, A.P., van Leenen, D., et al. (1999). Mammalian Cry1 and Cry2 are essential for maintenance of circadian rhythms. *Nature* 398, 627–630.
30. Albrecht, U., Sun, Z.S., Eichele, G., and Lee, C.C. (1997). A differential response of two putative mammalian circadian regulators, mper1 and mper2, to light. *Cell* 91, 1055–1064.
31. Sun, Z.S., Albrecht, U., Zhuchenko, O., Bailey, J., Eichele, G., and Lee, C.C. (1997). RIGUI, a putative mammalian ortholog of the *Drosophila* period gene. *Cell* 90, 1003–1011.
32. Takumi, T., Taguchi, K., Miyake, S., Sakakida, Y., Takashima, N., Matsubara, C., Maebayashi, Y., Okumura, K., Takekida, S., Yamamoto, S., et al. (1998). A light-independent oscillatory gene mPer3 in mouse SCN and OVLT. *EMBO J.* 17, 4753–4759.
33. Cho, W.K., Spille, J.H., Hecht, M., Lee, C., Li, C., Grube, V., and Cisse, I.I. (2018). Mediator and RNA polymerase II clusters associate in transcription-dependent condensates. *Science* 361, 412–415.
34. Henninger, J.E., Oksuz, O., Shrinivas, K., Sagi, I., LeRoy, G., Zheng, M.M., Andrews, J.O., Zamudio, A.V., Lazaris, C., Hannett, N.M., et al. (2021). RNA-mediated feedback control of transcriptional condensates. *Cell* 184, 207–225.e24.
35. Hnisz, D., Shrinivas, K., Young, R.A., Chakraborty, A.K., and Sharp, P.A. (2017). A phase separation model for transcriptional control. *Cell* 169, 13–23.
36. Robles, M.S., Cox, J., and Mann, M. (2014). In-vivo quantitative proteomics reveals a key contribution of post-transcriptional mechanisms to the circadian regulation of liver metabolism. *PLoS Genet.* 10, e1004047.
37. Leng, Y., Musiek, E.S., Hu, K., Cappuccio, F.P., and Yaffe, K. (2019). Association between circadian rhythms and neurodegenerative diseases. *Lancet Neurol.* 18, 307–318.
38. Tuin, I., Voss, U., Kang, J.S., Kessler, K., Rüb, U., Nolte, D., Lochmüller, H., Tischert, S., Claus, D., Krakow, K., et al. (2006). Stages of sleep pathology in spinocerebellar atrophy type 2 (SCA2). *Neurology* 67, 1966–1972.
39. Becker, L.A., Huang, B., Bieri, G., Ma, R., Knowles, D.A., Jafar-Nejad, P., Messing, J., Kim, H.J., Soriano, A., Auburger, G., et al. (2017). Therapeutic reduction of ataxin-2 extends lifespan and reduces pathology in TDP-43 mice. *Nature* 544, 367–371.
40. Duez, H., and Staels, B. (2009). Rev-erb-alpha: an integrator of circadian rhythms and metabolism. *J. Appl. Physiol.* (1985) 107, 1972–1980.
41. Theiss, C., and Meller, K. (2002). Aluminum impairs gap junctional intercellular communication between astroglial cells in vitro. *Cell Tissue Res.* 310, 143–154.
42. Kornhauser, J.M., Ginty, D.D., Greenberg, M.E., Mayo, K.E., and Takahashi, J.S. (1996). Light entrainment and activation of signal transduction pathways in the SCN. *Prog. Brain Res.* 111, 133–146.
43. Tahara, Y., and Shibata, S. (2016). Circadian rhythms of liver physiology and disease: experimental and clinical evidence. *Nat. Rev. Gastroenterol. Hepatol.* 13, 217–226.
44. Kumar, L., and E Futschik, M.E. (2007). Mfuzz: a software package for soft clustering of microarray data. *Bioinformatics* 2, 5–7.
45. Zhou, Y., Zhou, B., Pache, L., Chang, M., Khodabakhshi, A.H., Tanaseichuk, O., Benner, C., and Chanda, S.K. (2019). Metascape provides a biologist-oriented resource for the analysis of systems-level datasets. *Nat. Commun.* 10. <https://doi.org/10.1038/s41467-019-09234-6>.
46. Chen, C., Chen, H., Zhang, Y., Thomas, H.R., Frank, M.H., He, Y., and Xia, R. (2020). TBtools: an integrative toolkit developed for interactive analyses of big Biological Data. *Mol. Plant* 13, 1194–1202.
47. Kechin, A., Boyarskikh, U., Kel, A., and Filipenko, M. (2017). cutPrimers: a new Tool for accurate cutting of primers from reads of targeted next generation sequencing. *J. Comput. Biol.* 24, 1138–1143.
48. Dobin, A., Davis, C.A., Schlesinger, F., Drenkow, J., Zaleski, C., Jha, S., Batut, P., Chaisson, M., and Gingeras, T.R. (2013). STAR: ultrafast universal RNA-seq aligner. *Bioinformatics* 29, 15–21.
49. Anders, S., Pyl, P.T., and Huber, W. (2015). HTSeq—a Python framework to work with high-throughput sequencing data. *Bioinformatics* 31, 166–169.
50. Love, M.I., Huber, W., and Anders, S. (2014). Moderated estimation of fold change and dispersion for RNA-seq data with DESeq2. *Genome Biol.* 15, 550.
51. Xiao, Z., Zou, Q., Liu, Y., and Yang, X. (2016). Genome-wide assessment of differential translations with ribosome profiling data. *Nat. Commun.* 7, 11194.
52. Langmead, B., and Salzberg, S.L. (2012). Fast gapped-read alignment with Bowtie 2. *Nat. Methods* 9, 357–359.
53. Challis, R.C., Ravindra Kumar, S., Chan, K.Y., Challis, C., Beadle, K., Jang, M.J., Kim, H.M., Rajendran, P.S., Tompkins, J.D., Shivkumar, K., et al. (2019). Systemic AAV vectors for widespread and targeted gene delivery in rodents. *Nat. Protoc.* 14, 379–414.
54. Hutchison, A.L., Maienschein-Cline, M., Chiang, A.H., Tabei, S.M., Gudjonsson, H., Bahroos, N., Allada, R., and Dinner, A.R. (2015). Improved statistical methods enable greater sensitivity in rhythm detection for genome-wide data. *PLoS Comput. Biol.* 11, e1004094.
55. Choi, H.M.T., Schwarzkopf, M., Fornace, M.E., Acharya, A., Artavanis, G., Stegmaier, J., Cunha, A., and Pierce, N.A. (2018). Third-generation *in situ* hybridization chain reaction: multiplexed, quantitative, sensitive, versatile, and robust. *Development* 145, dev165753.

STAR★METHODS

KEY RESOURCES TABLE

REAGENT or RESOURCE	SOURCE	IDENTIFIER
Antibodies		
Anti-puromycin	Sigma-Aldrich	Cat# MABE343, RRID: AB_2566826
Anti-Ataxin-2 antibody	Proteintech	Cat# 21776-1-AP, RRID: AB_10858483
Anti-Ataxin-2L antibody	Proteintech	Cat# 24822-1-AP, RRID: AB_2879743
Anti-CLOCK	Abcam	Cat# ab3517, RRID: AB_303866
Anti-PER2	Abcam	Cat# ab179813, RRID: N/A
Anti-CRY1	Proteintech	Cat# 13474-1-AP, RRID: AB_10697652
Anti-EIF2A	Proteintech	Cat# 11233-1-AP, RRID: AB_2246321
Anti-EIF4B	Proteintech	Cat# 17917-1-AP, RRID: AB_2097541
Anti-RPL8	ABclonal	Cat# A10042, RRID: AB_2757564
Anti-RPS13	Proteintech	Cat# 16680-1-AP, RRID: AB_2182500
Anti-KDEL	Abcam	Cat# ab176333, RRID: AB_2819147
Anti-βIII-Tubulin antibody	ABclonal	Cat# A18132, RRID: AB_2861923
Goat anti-Mouse IgG (H+L) Secondary Antibody, HRP	Thermo Fisher Scientific	Cat# 31430, RRID: AB_228307
Goat anti-Rabbit IgG (H+L) Secondary Antibody, HRP	Thermo Fisher Scientific	Cat# 31460, RRID: AB_228341
Goat anti-Rabbit IgG (H+L) Cross-Adsorbed Secondary Antibody, Alexa Fluor™ 488	Thermo Fisher Scientific	Cat# A-11008, RRID: AB_143165
Goat anti-Rabbit IgG (H+L) Cross-Adsorbed Secondary Antibody, Alexa Fluor™ 594	Thermo Fisher Scientific	Cat# A-11012, RRID: AB_2534079
Goat anti-Rabbit IgG (H+L) Cross-Adsorbed Secondary Antibody, Alexa Fluor™ 647	Thermo Fisher Scientific	Cat# A32733, RRID: AB_2633282
Bacterial and virus strains		
DH5α <i>Escherichia coli</i>	This study	N/A
BL21-(DE3)-RPL <i>Escherichia coli</i>	This study	N/A
Chemicals, peptides, and recombinant proteins		
Dexamethasone	Macklin	D917754
Cycloheximide	Ameresco	94271
Sucrose	Ameresco	M117
Murine RNase inhibitor	Vazyme	R301
Protease Inhibitor Cocktail	Sigma-Aldrich	539134
Puromycin	Sigma-Aldrich	P8833
RNase I	Ambion	AM2295
TURBO™ DNase	Thermo Fisher Scientific	AM2238
TRIzol	Invitrogen Ambion	15596026
Propidium iodide	Thermo Fisher Scientific	P3566
Normal goat serum	Bioss	C01-03001
Ni-NTA Resin	GenScript	L00666
Alexa Fluor 488/568-C5-maleimide	Thermo Fisher Scientific	A10254
RIPA	Solarbio	R0010
T4 Polynucleotide Kinase	NEB	M0201L
CircLigase™ ssDNA Ligase	Lucigen	CL4115K
Sequence grade modified trypsin	Promega	V5111
RNA scope wash buffer	ACD	310091
0.25% Trypsin-EDTA	MACGENE	CC012.500
Polyethylenimine	YEASEN	40815ES03
Iodixanol	Sigma-Aldrich	D1556

(Continued on next page)

Continued

REAGENT or RESOURCE	SOURCE	IDENTIFIER
Proteinase K	Solarbio	P9460
Critical commercial assays		
Click-iT™ HPG Alexa Fluor™ 488 Protein Synthesis Assay Kit	Thermo Fisher Scientific	C10428
Hieff® III 1st Strand cDNA Synthesis SuperMix for qPCR	YEASEN	11141ES10
Hieff® qPCR SYBR Green Master Mix (No Rox)	YEASEN	11201ES08
RNAscope™ Multiplex Fluorescent V2 Assay	ACD	323100
RNAscope® Probe- Mm-Per2-C2	ACD	454521-C2
TNT® Quick Coupled Transcription/Translation Systems	Promega	L1171
Luciferase Reporter Gene Assay Kit	YEASEN	11401ES60
MEGAscript T7 Transcription Kit	Thermo Fisher Scientific	AM1334
Deposited data		
Mass Spectrum data of Cryo-mill IP	This study	Table S3
GO analysis of proteome in mass spectrometry	This study	Table S4
Data files for Ribo-seq	This study	GEO: GSE222433
Experimental models: Cell lines		
Human: osteosarcoma cell line U2OS	This study	N/A
Human: hypothalamic GnRH cell line GT1-7	This study	N/A
Human: neuroblastoma cell line SH-SY5Y	This study	N/A
Human: embryonic kidney cell line, HEK293T	This study	N/A
Human: liver epithelial cell line THLE-2	This study	N/A
Experimental models: Organisms/strains		
Mouse: B6/J.Vip-IRES-Cre	From Yi Zhong	N/A
Mouse: B6/JGpt-Atxn2 ^{em1Cflox} /Gpt	GemPharmatech	Strain NO. T052332
Mouse: B6/JGpt-Atxn2 ^{em3Cd4238} /Gpt	GemPharmatech	Strain NO. T016843
Oligonucleotides		
Guide RNAs (gRNAs) targeted to ATXN2: 5'-GTATTG GAAATACCCCCAGT-3'	This study	N/A
Guide RNAs (gRNAs) targeted to ATXN2L: 5'-CCCC GGATCTTAAAGGAGGA-3	This study	N/A
Primers for RT-PCR, see Table S3	This study	N/A
Sequences of UTR used in in vitro translation and RNA recruitment assay, see Table S5	This study	N/A
Primers for FISH, see Table S6	This study	N/A
Recombinant DNA		
pcDNA4TO-24×GCN4-v4-24×PP7	From Weirui Ma	N/A
pHR-scFv-GCN4-sfGFP-GB1-dWPRE	From Weirui Ma	N/A
pHis-ATXN2 LCD	This study	N/A
pHis-ATXN2L LCD	This study	N/A
pLVX-mCherry-ATXN2	This study	N/A
pLVX-EGFP-ATXN2	This study	N/A
T7-luciferase-PER2/CRY1/WFS1/RRBP1-3'UTR	This study	N/A
pAAV-hSyn-mCherry-IRES-Cre	From Yingqing Li	N/A
pAAV2/8	From Yingqing Li	N/A
pHelper	From Yingqing Li	N/A
Software and algorithms		
Mfuzz	Kumar and Futschik ⁴⁴	http://mfuzz.sysbiolab.eu/
MEGA-X	N/A	https://www.megasoftware.net/
Clustal W	N/A	https://www.genome.jp/tools-bin/clustalw

(Continued on next page)

Continued

REAGENT or RESOURCE	SOURCE	IDENTIFIER
Clustal Omega	N/A	https://www.ebi.ac.uk/Tools/msa/clustalo/
“RAIN” (R Package)	Thaben and Westermark ¹⁸	N/A
Metascape	Zhou et al., 2019 ⁴⁵	https://metascape.org/gp/index.html#/main
TB Tools	Chen et al. ⁴⁶	N/A
Cutadapt	Kechin et al. ⁴⁷	N/A
Fastx quality filter	N/A	http://hannonlab.cshl.edu/fastx_toolkit/
FastQC	N/A	http://www.bioinformatics.babraham.ac.uk/projects/fastqc/
STAR	Dobin et al. ⁴⁸	N/A
HTSeq-count	Anders et al. ⁴⁹	N/A
DESeq2	Love et al. ⁵⁰	N/A
Xtail	Xiao et al. ⁵¹	https://github.com/xryanglab/xtail
LumiCycle Software	Actimetrics, Wilmette, IL	N/A
Clocklab software	Actimetrics, Wilmette, IL	N/A
Other		
Cell ultrasonic crusher	SCIENTZ	JY98
Amicon filter	Millipore	UFC903096
Spin desalting columns	Cytiva	28918006PD
Trap column for mass spectrum	Thermo Fisher Scientific	164535

RESOURCE AVAILABILITY**Lead contact**

Further information and requests for resources and reagents should be directed to and will be fulfilled by the lead contact, Dr. Yi Lin (linyi@mail.tsinghua.edu.cn).

Materials availability

This study did not generate new unique reagents. Plasmids generated in this study are available upon request.

Data and code availability

- Mass spectra data used in the manuscript are available in supplemental information files. Microscopy data reported in this paper will be shared by the **lead contact** upon request. The Ribo-seq datasets generated in this study are available in the GEO database repository (GEO: GSE222433).
- This paper does not report original code.
- Any additional information required to reanalyze the data reported in this paper is available from the **lead contact** upon request.

EXPERIMENTAL MODEL AND STUDY PARTICIPANT DETAILS**Cell lines**

The human osteosarcoma cell line U2OS, hypothalamic GnRH cell line GT1-7, neuroblastoma cell line SH-SY5Y, human embryonic kidney cell line HEK293T, and human liver epithelial cell line THLE-2 were used in this study. All human cell lines were cultivated in Dulbecco’s Modified Eagle Medium (DMEM, GIBCO, C11995500CP), supplemented with 10% fetal bovine serum (Mediatech, 35-081-CV) and 1% penicillin and streptomycin (Hyclone, SV30010), and maintained at 37°C with 5% CO₂.

CRISPR KO cell lines

Guide RNAs (gRNAs) targeting the *ATXN2* gene (5'-GTATTGGAAATCCCCAGT-3') and the *ATXN2L* gene (5'-CCCGGGATCT TAAAGGAGGA-3') were designed using the online software Benchling (<https://benchling.com/editor>). The guide RNA sequences were then cloned into the pX459 vector following the protocols established in the Zhang lab’s CRISPR Genome Engineering Toolbox.

Following transfection, cells were cultured in the presence of 1 µg/mL puromycin for 3 days to select for knockout clones. Single colonies were harvested and the KO cells were verified by western blotting, immunostaining against the targeted protein, and sequencing.

Mouse models

Atxn2^{-/-} mice (Strain NO. T016843) and *Atxn2*^{flox/flox} mice (Strain NO. T052332) were purchased from GemPharmatech (Nanjing, China). Vip-IRES-Cre mice were generously provided by the laboratory of Dr. Yi Zhong, Tsinghua University. C57BL/6J controls of the same age were obtained from Laboratory Animal Resources Center, Tsinghua University.

All animal experiments described in this study were conducted in accordance with the guidelines and approved by the Institutional Animal Care & Use Committee of Tsinghua University and the Animal Welfare and Ethics Committee of Tsinghua University. The animals used in this study were of both genders and within an age range of 2–4 months. All mice were housed in pathogen-free barrier facilities. Wild-type, *Atxn2* knockout (*Atxn2*^{+/-} and *Atxn2*^{-/-}), and *Atxn2l* tissue-specific Cre-driver knockout mice (*Atxn2l*^{flox/+} and *Atxn2l*^{flox/flox}) of the same age were randomly selected for experiments. Corresponding primers utilized for genotyping were listed in Table S2.

METHOD DETAILS

Protein synthesis assay using Click-iT HPG system

U2OS cells were synchronized using 200 nM dexamethasone for two hours. The medium was then replaced with dexamethasone-free DMEM. To prepare the Click-iT HPG working solution, a stock solution was diluted 1:1000 in pre-warmed L-methionine-free medium to achieve a final HPG concentration of 50 μM. Thirty minutes prior to the designated time, the culture medium was replaced with the HPG working solution. After 30 minutes of incubation at 37°C, cells were washed once with PBS and fixed with 4% formaldehyde. The Alexa Fluor 488 azide was then conjugated to HPG through click reaction. The HPG-incorporated proteins were subsequently detected using confocal microscopy.

Polysome profiling

The 10% and 50% sucrose solutions were prepared in polysomal buffer containing 20 mM Tris-HCl pH 7.4, 15 mM MgCl₂, 150 mM NaCl in RNase-free conditions. The BioComp model 108 Gradient Master was utilized to prepare a 10%-50% sucrose gradient for polysome isolation. For cultured U2OS cells, one 15 cm dish was treated with 0.1 mg/mL cycloheximide for 10 minutes. The cells were rinsed twice with 0.1 mg/mL cycloheximide in 1× PBS, collected, and resuspended in a polysome lysis buffer composed of 20 mM Tris-HCl pH 7.5, 15 mM MgCl₂, 150 mM NaCl, 1% Triton X-100, 0.1 mg/mL cycloheximide, 1 mM DTT, 2 U/μL Murine RNase inhibitor, and 1× protease inhibitors. The solution was incubated for 10 minutes on ice and then centrifuged for 10 minutes at 12,000 g at 4 °C. Clear supernatants from lysed cells were loaded onto the 10-50% sucrose gradients and centrifuged at 36,000 rpm, 4 °C for 120 minutes using a Beckman SW41 rotor.

For mouse brain and liver tissues, 50 or 20 mg tissue powder was lysed with polysome lysis buffer, respectively. After incubation for 20 minutes on ice, the resuspension solution was centrifuged for 10 minutes at 12,000 g at 4 °C. Supernatants from lysed tissues were loaded onto the 10-50% sucrose gradients and centrifuged at 36,000 rpm, 4 °C for 120 minutes using a Beckman SW41 rotor.

ISCO gradient fractionation system (ISCO Model 160 Gradient Former Foxy Jr. Fraction Collector) was used to isolate sucrose gradient fractions, and the abundance of ribosomal RNA was visualized by monitoring the absorbance at 254 nm.

Surface sensing of translation (SUnSET) assay

The SUnSET assay was used to measure mRNA translation rates by measuring the degree of puromycin incorporation. In this assay, cells were synchronized with DXMS, and then replaced with fresh medium containing 1 μg/mL puromycin at different time points. After incubation for 30 min at 37°C, cells were washed with ice-cold 1×PBS and lysed with RIPA buffer (50mM Tris pH 7.4, 150mM NaCl, 1% Triton X-100, 1% sodium deoxycholate, 0.1% SDS). Similarly, in mouse liver tissues, 100 μL of a 20 mM solution of puromycin in PBS was injected intraperitoneally into 8-week-old mice, and after 1 hour, tissues were harvested, snap-frozen in liquid nitrogen, cryogenically ground into powder with a pestle, and lysed with RIPA buffer. The protein concentration was measured using BCA protein assay, and protein lysates were analyzed by SDS-PAGE and western blotting using anti-puromycin antibody to detect the degree of puromycin incorporation.

To measure the rate of protein synthesis in mice brains, puromycin was stereotactically injected into the left ventricle of the mouse brain. Mice were anesthetized with isoflurane and immobilized using a stereotactic frame equipped with a heating blanket to maintain body temperature throughout the procedure. After hair removal and cleaning of the shaved area with betadine and alcohol, a small incision was made to expose the skull surface, and a small hole was drilled into the skull to allow injection of 3 μL puromycin (10 mg/mL) using a nanoliter microinjection pump. The injection speed was pump-controlled at 0.2 μL/min. The needle was left in place for 10 min before it was slowly withdrawn. One hour after injection, mice were perfused with saline followed by 4% paraformaldehyde (PFA), and the brain was immediately removed, fixed in 4% PFA for immunofluorescence analysis. Sagittal brain sections were stained with the primary antibody against puromycin overnight at 4°C, and then fluorescence-conjugated secondary antibodies (Alexa Fluor 594) were incubated at room temperature in darkness for 1 hour, followed by staining with DAPI. Images were acquired using an Olympus IXplore spinning disk microscope.

Phylogenetic tree construction

To obtain the orthologs of the ATXN2 and ATXN2L proteins, we searched for homologous sequences in several organisms including *Saccharomyces cerevisiae*, *Drosophila melanogaster*, *Caenorhabditis elegans*, and metazoans using the National Center for Biotechnology Information (<https://www.ncbi.nlm.nih.gov/>) and EnSDbI (<https://asia.enSDbI.org/index.html>) websites. The resulting ATXN2/ATXN2L orthologous proteins (Table S1) were used to construct a phylogenetic tree. The amino acid sequences were aligned using the Clustal W program and the phylogenetic tree was constructed using MEGA-X software, with the neighbor-joining method and 1,000 times bootstrap replications.

Ribosome profiling (Ribo-seq) library preparation and sequencing

For each sample, one 15 cm dish of U2OS cells was treated with 0.1 mg/mL cycloheximide at 37°C for 1 minute. The cells were then rinsed once with ice-cold PBS containing 0.1 mg/mL cycloheximide, and subsequently scraped and harvested in 300 µL of lysis buffer (20 mM Tris-HCl pH 7.4, 150 mM NaCl, 5 mM MgCl₂, 1% Triton X-100, 1 mM DTT, 25 U/mL TURBO DNase and 0.1 mg/mL of cycloheximide). The cell lysate was incubated on ice for 10 minutes and then clarified by centrifugation at 20,000 rcf for 5 minutes at 4°C. The RNA concentration of the clarified lysate was determined by measuring the absorbance at 260 nm using a spectrophotometer.

To generate ribosome-protected fragments (RPFs), the cell lysate was digested with 90 U per A260/mL (A260 of cell lysate minus A260 of lysis buffer) of RNase I for 30 minutes at 4°C with gentle rotation. The digested cell lysate was then overlaid onto a 1 M sucrose cushion and the ribosomes were pelleted by centrifugation at 70,000 rpm for 2 hours at 4°C in a Beckman 90Ti rotor. The ribosome pellets were then dissolved in 1 mL of TRIzol reagent and RNA samples were purified according to the manufacturer's instruction. The RNA samples were separated on a 15% (wt/vol) polyacrylamide TBE-urea gel and gel slices corresponding to 26-34 nt were excised. The RPFs were recovered by adding 0.4 mL of RNA extraction buffer (400 mM ammonium acetate, 0.05% SDS) to disrupted gel slices, rotating at room temperature overnight and precipitating with isopropanol.

Total RNA samples were heat-fragmented for 20 minutes at 94°C with T4 polynucleotide kinase buffer (NEB). Next, both fragmented total RNA samples and RPFs were subjected to library preparation. In brief, RNA samples were end-repaired with T4 PNK and ligated with a pre-adenylated 3' adaptor, followed by cDNA synthesis and purification. The cDNA was then subjected to circularization by CircLigase ssDNA ligase and the libraries were indexed during PCR amplification. The libraries were pooled and sequenced on an HiSeq X Ten platform and 150 bp paired-end reads were generated. The sequencing was performed by Annoroad Gene Technology Co., Ltd.

RNA-seq and Ribo-seq data processing and analysis

The adaptor sequence (5'-CTGTAGGCACCATCAAT-3') was removed from both mRNA and Ribo-seq data using Cutadapt,⁴⁷ and low-quality reads were discarded using fastx quality filter (http://hannonlab.cshl.edu/fastx_toolkit/). Quality control was conducted using FastQC (<http://www.bioinformatics.babraham.ac.uk/projects/fastqc/>). Contamination from ribosomal RNA was identified by aligning reads to human rRNA sequences using Bowtie,⁵² and mapped reads were removed from subsequent analysis. Reads with a length of 25-35 nt were retained for ribosome profiling analysis. The remaining reads were mapped to the human reference genome asSDbly (GRCh38) using STAR,⁴⁸ with the annotation file (Homo_sapiens.GRCh38.88.gtf) downloaded from the EnSDbI genome browser, and the following parameters: (-alignEndsType EndToEnd -outFilterMismatchNmax 1 -outFilterMultiMapNmax 5 -quantMode TranscriptomeSAM GeneCounts).

RNA-seq reads were counted using HTSeq-count⁴⁹ in intersection-strict mode, while RPF reads were counted using a custom Python script from Xiao.⁵¹ Raw counts of ribosome footprints and RNA were normalized using DESeq2⁵⁰ to eliminate the bias of sequencing depth among different libraries. Normalized RPF counts were further normalized by the sums of mitochondrial RPF. RPF count was divided by RNA count to get translation efficiency. Statistical analysis of differentially transcribed genes within each pair of samples was performed using the R package Xtail.⁵¹

Apoptosis assay by flow cytometry

Cells were first seeded into 35 mm dishes and synchronized with 200 nM dexamethasone (DXMS) for two hours. Apoptosis was then evaluated by flow cytometry analysis using an Annexin V-FITC apoptosis detection kit (Solarbio, CA1020) using Annexin V-FITC staining with propidium iodide (PI). The synchronized cells were then washed in cold PBS and digested at eight-hour intervals for a total of 24 hours, with two replicates per time point. After digestion, the cells were centrifuged and resuspended in binding buffer. Cells were stained with FITC-labeled annexin and analyzed by flow cytometry. For double staining, PI was added 5 minutes before flow cytometric analysis using CytoFlex LX flow cytometer.

Cell proliferation assay

In this experiment, cells of different genotypes (WT, ATXN2 KO, ATXN2L KO, and ATXN2/2L DKO) were seeded into 48-well plates at a starting density of 12,000 cells per well. After 12 hours of seeding, cells were treated with 200 nM DXMS for two hours to synchronize the cells. Then, the medium was replaced with fresh medium without DXMS, and the real-time cell proliferation was monitored using the IncuCyte live-cell analysis system (ESSEN Bioscience).

The cell proliferation ability was measured by quantifying the cell confluence of cell images over time. The proliferation curves were plotted by calculating the fold change (FC) in cell confluence at different time points compared to the confluence at time 0. The experiment aimed to compare the cell proliferation ability of cells with different genotypes under these conditions.

Cell cycle analysis with flow cytometry

The U2OS cells were synchronized with DXMS and then stained with Hoechst 33342 to monitor their cell cycle progression over a 24-hour period. The staining was performed by adding 1 µg/mL of Hoechst 33342 to the cells and incubating for 30 minutes. The cells were then washed three times with PBS and collected at an eight-hour interval for 24 hours, with 2 replicates per time point. The cells were collected and the supernatant was removed by centrifugation at 1000 rpm for 5 minutes. The cell pellets were resuspended in cold PBS and cell cycle analysis was performed using a 405nm UV laser and the CytoFlex LX flow cytometer.

Quantitative real-time PCR

Total RNA was extracted from cultured cells or dissected tissues using TRIzol (Invitrogen Ambion, Shanghai) according to the manufacturer's protocol. Reverse transcription was performed using Hifair® III 1st Strand cDNA Synthesis SuperMix for qPCR (YEASEN). Quantitative reverse transcription-PCR (qRT-PCR) was carried out on a Bio-Rad CFX96 or Roche LightCycler® 480 thermal cycler with gene-specific primers (Table S2) and SYBR green supermix. The ΔΔCT method was used for quantitative analysis, with Actin as the endogenous control.

For AAV titration, virus particles were lysed with proteinase K, and a portion of the WPRE element was amplified using the WPRE-F and WPRE-R primers (Table S2). pAAV plasmids containing the Cre sequence were used as a standard stock, as previously described.⁵³

Immunofluorescence (IF)

The cells grown on glass-bottomed confocal dishes were fixed with a 4% paraformaldehyde solution for 15 minutes, permeabilized with 0.5% Triton X-100 in phosphate-buffered saline (PBS) for 15 minutes, and blocked with 10% normal goat serum for 30 minutes at room temperature.

For staining mouse tissue sections, the animals were deeply anesthetized with Avertin and then perfused intracardially with ice-cold 0.01 M PBS, followed by 4% PFA in PBS (pH 7.4). The brain and liver were dissected and post-fixed overnight at 4°C in 4% PFA. The tissues were rinsed with PBS and then transferred into 30% sucrose in PBS for 24 hours. After that, they were frozen on dry ice and embedded in OCT. Coronal sections of the brain (14 µm) or liver (7 µm) were cut with a cryostat (Leica, CM3050S) at -20°C. The tissue sections were permeabilized with 0.5% Triton X-100 in PBS for 30 minutes at room temperature and blocked with 10% normal goat serum for 1 hour at room temperature.

The cells and tissue sections were stained with a primary antibody against ATXN2 (Proteintech, 21776-1-AP) or ATXN2L (Protein-tech, 24822-1-AP) overnight at 4°C. The corresponding fluorescence-conjugated secondary antibodies (Alexa Fluor 488/594, Thermo Fisher Scientific, goat anti-rabbit) were then incubated at room temperature in darkness for 1 hour. The cells and tissues were then stained with DAPI. Images were acquired using a Nikon AX confocal microscope and Olympus IXplore spinning disk microscope.

Immunogold electron microscopy

White adipose tissue (WAT) and liver were fixed in a solution containing 3% formaldehyde and 0.2 M sucrose in 0.1 M Sorensen's phosphate buffer (pH=7.2). The tissue samples were then sliced and processed by the University of Michigan Microscopy Core. Ultra-thin sections (80 nm) were cut, placed on bare nickel grids, and stored at 4°C. For immunogold labeling, the grids were quenched in 80 mM glycine and incubated in a blocking solution (EMS 25599) containing 0.2% Tween-20 for 1 hour at room temperature. Next, the grids were incubated overnight with primary antibodies at 4°C in a humidification chamber. The grids were then incubated with 18 nm colloidal gold antibodies (1:25 v/v, Jackson ImmunoResearch 711-215-152) for 1 hour at room temperature, followed by post-fixation in 1% glutaraldehyde and contrast staining using 0.5% uranyl acetate. After carbon evaporation, the grids were imaged using a JEOL electron microscope at the University of Michigan Microscopy Core.

Protein conservation analysis

The protein sequences of ATXN2 and ATXN2L orthologs were retrieved from EnSDbl (<https://www.enSDbl.org/>, version 107, 2022-08-16) for 200 species. Multiple sequence alignments (MSA) were conducted using Clustal Omega (<https://www.ebi.ac.uk/Tools/msa/clustalo/>) with the default settings. Protein site conservation scores were calculated using ConSurf with a Bayesian model and default settings.

Protein expression and purification

The coding sequences of ATXN2 LCD (amino acids 1125–1312), ATXN2L LCD (amino acids 875–1075), FUS LCD (amino acids 1–214) and YTHDC1 LCD (amino acids 494–727) were amplified from human cDNA and cloned into pHis-parallel vector with an N-terminal 6×His tag. All ATXN2 LCD mutations were introduced by site-directed mutagenesis. Recombinant proteins were expressed using BL21-(DE3)-RIPL *Escherichia coli* cells. Briefly, BL21(DE3) cells were transformed with corresponding plasmids and plated on LB

agar with ampicillin selection, overnight at 37°C. Single colonies were inoculated into a 5 mL LB culture and grown overnight at 37°C in a shaker at 220 rpm. The culture was added to 1 L of LB media and grown at 37°C until the OD₆₀₀ reached 0.6. Cells were induced with 0.5 mM IPTG at 37°C for 4 hours at 220 rpm and harvested by centrifuging at 4,000 rpm for 25 minutes at 4°C. The pellet was resuspended in denaturing lysis buffer (20 mM Tris-HCl pH 7.4, 200 mM NaCl, 6 M Guanidine-HCl, 0.1 mM PMSF, 20 mM β-Mercaptoethanol, and protease inhibitor cocktail and then sonicated for 20 minutes (10 s on / 10 s off, 180 W) with a cell ultrasonic crusher. After centrifugation at 20,000 g for 40 minutes, the supernatant was collected and loaded onto Ni-NTA Resin for 30 minutes at 4°C. The Ni-NTA Resin was washed with wash buffer (20 mM Tris-HCl pH 7.4, 200 mM NaCl, 6 M Guanidine-HCl, 0.1 mM PMSF, 20 mM β-Mercaptoethanol, and 20 mM imidazole) and eluted with elution buffer (200 mM NaCl, 20 mM Tris-HCl pH 7.4, 6 M Guanidine-HCl, 0.1 mM PMSF, 20 mM β-Mercaptoethanol, and 300 mM imidazole). The purified proteins were further concentrated to 2-4 mM using an Amicon filter (Millipore). The purity of all proteins was confirmed by SDS-PAGE.

To label the purified proteins with fluorescent dyes, 200 ng/mL Alexa Fluor 488/568-C5-maleimide (Thermo Fisher Scientific) was added, and the mixture was incubated in the dark for 1 hour on ice. Spin desalting columns (Cytiva) were used to remove free dyes. After equilibration, protein samples were loaded onto the desalting column and centrifuged at 2,000 g for 1 minute at 4°C. The proteins flowing through the column were collected for future use.

In vitro phase separation assays

The phase separation assay was conducted using glass bottom 384-well plates. The purified proteins were diluted into a gelation buffer containing NaCl in the range of 50-1000 mM and 20 mM Tris-HCl pH 7.4 to achieve the final protein concentration (2.5-120 μM for ATXN2 LCD, 10-80 μM for ATXN2L LCD, 60 μM for FUS LCD, 65 μM for YTHDC1). The resulting phase-separated droplets were added to a 384-well plate and allowed to settle for 30 minutes at room temperature. Images of the condensates were captured using an Olympus IXplore spinning disk microscope.

Fluorescence recovery after photobleaching (FRAP) measurements

To evaluate the fluidity of the phase-separated droplets formed by ATXN2 and ATXN2L LCD, we performed *in vitro* fluorescence recovery after photobleaching (FRAP) experiments using a Nikon A1 HD25 confocal microscope. The protein condensates were bleached with a laser pulse of either 561 nm or 488 nm, and the recovery of fluorescence intensity was recorded for 500 s with 5 s intervals for ATXN2 LCD and for 360 s with 10 s intervals for ATXN2L LCD. The fluorescence intensity of the bleached region was analyzed using NIS-Elements AR 5.4 software, and the recovery curve indicating changes in fluorescence intensity over time was plotted using GraphPad Prism. Six parallel replicates were conducted in side-by-side subcolumns, and the data are presented as mean ± standard deviation (SD).

Western blot

Cells were lysed with RIPA buffer for half an hour on ice and clarified by centrifugation at 4°C, 12,000 rpm for 5 minutes. Mouse tissues were first frozen in liquid nitrogen and then homogenized to a fine powder. The lysates were obtained by sonicating the tissues in RIPA buffer at 90 W for 10 seconds followed by centrifugation. 10 or 20 μg of protein samples were resolved by SDS-PAGE on 8% or 12% polyacrylamide gels and transferred onto PVDF membranes. The membranes were incubated with specific primary antibodies overnight at 4°C. The blots were then incubated with secondary antibodies conjugated with peroxidase (whole molecule, Thermo Fisher Scientific) for 1 hour at room temperature. After washing the membranes thrice with TBS-T (10 mM Tris-HCl pH 7.4, 0.15 M NaCl, 0.05% Tween-20) for 5 minutes each time, the protein bands were visualized by chemiluminescence using a Tanon 4800 Multi imaging system. The band intensities were quantified using ImageJ Software.

Cryo-mill immunoprecipitation

U2OS cells were subjected to synchronization with 200 nM DXMS for two hours, followed by harvesting and cryogenic freezing at four-hour intervals over a period of 24 hours (3 replicates per time-point). Frozen cells were subsequently ground into a fine powder and resuspended in 2 volumes of lysis buffer consisting of 20 mM HEPES/KOH pH 7.4, 150 mM NaCl, 0.1% (w/v) NP-40, 0.1% (w/v) Tween-20, 1 mM DTT, 2% (v/v) glycerol, and 1/100 (v/v) protease inhibitor cocktail (Sigma Aldrich). The cell lysates were briefly sonicated and centrifuged at 20,000 g for 10 minutes. Magnetic Protein A/G beads conjugated to ATXN2 antibody were added to the cell lysate at a concentration of 400 μg beads per 0.1 gram of frozen cell powder, and incubated for 5 minutes at 4°C. The beads were washed thrice with 1 mL of lysis buffer. The proteins were eluted using 0.2 M glycine (pH 2.0). Samples were loaded with 6× protein loading buffer and incubated at 95°C for 20 minutes prior to mass spectrometry (LC-MS/MS) analysis.

Mass spectrometry data collection and analysis

Proteins that coimmunoprecipitated with ATXN2 were separated on 1D-SDS PAGE. The corresponding gel lane was excised, reduced with 10 mM of TCEP, and alkylated with 40 mM chloroacetamide. In-gel digestion was carried out using sequence-grade modified trypsin (Promega) in 50 mM ammonium bicarbonate at 37°C overnight. The resulting peptides were extracted twice with 1% trifluoroacetic acid in a 50% acetonitrile aqueous solution for 30 minutes. The extractions were then centrifuged in a speedVac to reduce the volume.

An UltiMateTM 3000 RSLCnano system, directly interfaced with a Q Exactive HF-X mass spectrometer, was used for LC-MS/MS analysis. Peptides were loaded onto a trap column (75 μm \times 20 mm, 3 μm C18, 100 Å, Thermo Fisher Scientific) with a maximum pressure of 620 bar using mobile phase A (0.1% formic acid in H₂O). They were then separated on an analytical column (100 μm inner diameter, packed in-house with ReproSil-Pur C18-AQ 1.9 μm resin from Dr. Maisch GmbH) with a gradient of 4-70% mobile phase B (80% acetonitrile and 0.08% formic acid) at a flow rate of 250 nL/min for 120 minutes. The MS analysis was operated in data-dependent acquisition (DDA) mode, with one full scan (300-1800 m/z, Resolution = 60,000 at 200 m/z) at automatic gain control (AGC) of 3e6 with a maximum injection time (IT) of 20 ms. This was followed by top 40 MS/MS scans with high-energy collision dissociation (AGC of 2e5, maximum IT 100 ms, isolation window 0.4 m/z, normalized collision energy of 32%, Resolution = 45,000 at 200 m/z).

For proteomics data analysis, the MS/MS data were searched against the Uniprot mouse database using the SEQUEST search engine in Proteome Discoverer 2.3 software. The search criteria required full tryptic specificity, allowed for two missed cleavages, and set carbamidomethylation (C) as the fixed modification. Oxidation (M) and acetylation (protein N-terminal) were set as variable modifications. Precursor ion mass tolerances were set at 10 ppm for all MS acquired in an Orbitrap mass analyzer, and the fragment ion mass tolerance was set at 20 mmu for all MS2 spectra acquired. The false discovery rate was set to 0.01 for peptides and determined by searching a reverse database. Relative protein quantification was calculated as the median of all possible pairwise peptide ratios (Table S3).

Bioinformatic and statistical analyses of proteomics data

For the proteomics analysis of wild-type U2OS cells based on their temporal protein expression patterns over 24 hours, we utilized the fuzzy c-means clustering algorithm and identified seven distinct groups of genes. The centers of each cluster are denoted by blue lines on the graph, while the y-axis represents normalized protein abundance. We conducted fuzzy cluster analysis of proteomic data using the R package Mfuzz,⁴⁴ and removed genes with missing values at six time points prior to clustering. The abundance values of the remaining genes were Z-score transformed before fuzz c-means clustering.

We employed the R package RAIN¹⁸ to detect rhythmic proteins using a period of 24 hours, a period-delta of 4, and a p-value cutoff of <0.05. The RAIN algorithm is an improved version of JTK-Cycle that provides superior sensitivity in rhythmicity analysis by detecting both symmetric and nonsymmetric rhythms.⁵⁴ Rhythmic proteins were classified by phases anticipated by RAIN, and the frequency distribution of cycling candidates in different phases was visualized using rose plots generated by ggplot2 (<https://rddocumentation.org/packages/ggplot2/versions/3.3.6>).

We performed Gene Ontology (GO) analysis using all ATXN2-associated proteins and the rhythmic proteins with peaks at different time points separately (p-value \leq 0.05) using metascape (<https://metascape.org/gp/index.html#/main>). Translation-related proteins, translation initiation factors, and ribosome components were sorted, and the temporal abundance profiles of each protein at different time points were visualized as heatmaps using TB Tools.⁴⁶ Enriched GO terms were visualized in a bubble plot using ggplot2. Additionally, we clustered ATXN2 immunoprecipitated proteins with a peak at 16 hours using STRING (<https://cn.string-db.org/>) and Cytoscape.

Cellular puncta analysis

To determine whether ATXN2 form cellular puncta in the representative images from various cell lines, the stained images were reconstructed using MATLAB. Specifically, the *imread()* function was utilized to read the image and generate a three-dimensional variable, where the first two dimensions represent the size of the image and the last dimension records the gray intensity of the protein-associated color channels. The *rgb2gray()* function was then used to read the gray value of the image. To standardize the image parameters, the images were converted into double class and the dimensions were set to 400x400, which corresponds to the length and width of our images. The *meshgrid()* program was employed to transform and visualize two-dimensional array variables into three dimensions. Finally, the *mesh()* function overlaid the 3D result from the previous step with the 2D image for analysis.

Purification of human 80S ribosomal subunits

HEK 293T cells were cultured and treated with 0.1 mg/mL cycloheximide for 10 minutes at 37°C and 5% CO₂. The cells were then washed twice with 0.1 mg/mL cycloheximide in 1× PBS. After that, cells were resuspended in lysis buffer consisting of 20 mM Tris-HCl pH 7.4, 15 mM MgCl₂, 50 mM KCl, 0.5 mM EDTA, 1% Triton X-100, 0.1 mg/mL cycloheximide, 2 mM DTT, 2 U/ μL Murine RNase inhibitor, and 1× protease inhibitors. The samples were incubated on ice for 10 minutes and then centrifuged at 12,000 g at 4°C for 10 minutes. The supernatant was loaded onto a 9 mL sucrose cushion (20 mM Tris pH 7.5, 15 mM MgCl₂, 50 mM KCl, 0.5 mM EDTA, 34% sucrose, 2 mM DTT, and 2 U/ μL Murine RNase inhibitor) in a 16 mm \times 76 mm polycarbonate ultracentrifuge tube. Crude ribosomes were pelleted by centrifugation at 70,000 rpm for 2 hours using a Beckman 90Ti rotor. The resulting pellet was slowly homogenized at 4°C in lysis buffer. Crude ribosomal subunits were further purified using a 10-40% sucrose gradient, which was prepared in ribosomal fraction buffer (sucrose diluted in buffer containing 15 mM Tris-HCl pH 7.4, 15 mM MgCl₂, and 300 mM NaCl, prepared under RNase-free conditions) using BioComp Gradient Master. The crude subunits were loaded onto the gradient and centrifuged at 36,000 rpm (Beckman SW41Ti rotor) for 2 hours at 4°C. Fractions were collected from top to bottom using BioComp Piston Gradient Fractionator. The sample absorbance was recorded using a UV reader and the fractions corresponding to 80S were pooled for a third-time purification. A final concentration of 10.5% PEG 20,000 was slowly added to the pooled fractions, which were then incubated on ice for 10 minutes and centrifuged at 10,000 rpm, 4 °C, for 10 minutes. The purified 80S ribosome was finally

resuspended in 200 µL buffer containing 150 mM NaCl, 20 mM Tris-HCl pH 7.4, and 1× protease inhibitors, to a final concentration of 5 mg/mL.

LLPS *in vitro* recruitment assays

The purified 80S ribosome solution was added to a phase separation buffer containing 25 mM Tris-HCl pH 7.5 and 150 mM NaCl, resulting in a final concentration of 0.5 mg/mL. Purified proteins, including ATXN2 LCD, ATXN2L LCD, FUS LCD, and YTHDC1 LCD, were then diluted at a 1:50 ratio into this 80S-containing buffer, resulting in final concentrations of 40 µM for ATXN2 LCD, ATXN2L LCD, and FUS LCD, and 20 µM for YTHDC1 LCD. The resulting condensates were then allowed to settle in a 384-well plate for 30 minutes at room temperature, and images of the condensates were captured using an Olympus IXplore spinning disk microscope.

To test RNA recruitment, the DNA sequences of *PER2* 5'UTR and 3'UTR, *FAM199X* 3'UTR, *BMAL1* 3'UTR, *CLOCK* 3'UTR, *PER1* 3'UTR, *CRY1* 3'UTR, *CRY2* 3'UTR, *WFS1* 3'UTR, and *RRBP1* 3'UTR (as listed in Table S5) were amplified via PCR from cDNA extracted from HEK293T cells using a 5' primer containing a T7 RNA Polymerase promoter sequence (5'-TAATACGACTCACTA TAGGG-3'). The target RNA fragments were obtained through an *in vitro* transcription kit (Thermo Fisher Scientific). Subsequently, Turbo DNase was added to eliminate the DNA template, and the RNA was then labeled with red fluorescence using propidium iodide. The RNA was then mixed with propidium iodide at a ratio of 1:5 and diluted to a concentration of 250 ng/µL with the phase-separated dilution buffer (25 mM Tris-HCl pH7.5, 150 mM NaCl). The phase-separating proteins were added to the system with a final protein concentration of 50 µM. The protein-RNA mixture was incubated for 30 minutes at room temperature, and images of the condensates were taken using the Olympus IXplore spinning disk microscope.

RNA fluorescence *in situ* hybridization

All the reagents used for RNA fluorescence *in situ* hybridization were obtained from the RNAscope™ Multiplex Fluorescent V2 Assay (ACD). Mouse brain sections were treated with hydrogen peroxide at room temperature for 10 minutes. The slides were then subjected to target retrieval using RNAscope 1X Target Retrieval Reagent at 99°C for 15 minutes. After treatment with RNAscope Protease III for 10 minutes, the brain tissues were placed into the HybEZ Oven and hybridized with a Mouse-*Per2* probe for 2 hours at 40°C. The slides were washed twice with pre-warmed wash buffer (ACD). Subsequently, the probe signals were amplified using the AMP solutions and labeled with the fluorophores Opal 690. Following multiple washes, the slides were stained with immunofluorescence.

Single-molecule fluorescent *in situ* hybridization in combination with immunocytochemistry

The hypothalamic GbRH GT1-7 cells were cultured on cover glass in a 24-well plate and fixed with 4% PFA for 15 minutes at room temperature. The cells were then stored in 1× PBS containing 0.5% bovine serum albumin (BSA). For the hybridization chain reaction assay (HCR), public codes were used to design the *Per2* probes that targeted the mRNA sequence. The probe sequences were synthesized by Sangon Biotech, China and are listed in Table S6.

For HCR, cells were first permeabilized in 70% ethanol for 16 hours at 4°C, followed by treatment with 0.5% Triton X-100 in 1× PBS at 37°C for 30 minutes. The cells were then washed with 1× PBS at room temperature and pre-hybridized in 30% probe hybridization buffer for 15 minutes at 37°C, followed by incubation in 30% probe hybridization buffer containing *Per2* probes at 37°C for 3 hours. After mRNA hybridization, the washing and amplification steps were performed as previously described.⁵⁵

For the immunocytochemistry assay, staining was further conducted on the HCR-labeled sections. The HCR-labeled sections were first blocked with 10% donkey serum in 1× PBS for 1 hour, then incubated with ATXN2 antibody diluted in 1× PBS solution containing 1% donkey serum, 1% BSA, and 0.1% Triton X-100 for 12 hours at 4°C. The cells were then washed with 1× PBS three times and stained with a secondary antibody for 2 hours at room temperature. Finally, the stained cells were mounted on glass slides for further imaging using an Olympus IXplore spinning disk microscope.

In vitro translation assay

The *in vitro* translation assay was performed using the TNT® Quick Coupled Transcription/Translation Systems (Promega). To create the plasmids T7-luciferase-PER2-3'UTR, T7-luciferase-CRY1-3'UTR, T7-luciferase-WFS1-3'UTR, and T7-luciferase-RRBP1-3'UTR (Table S5), the corresponding 3'UTRs were inserted downstream of the luciferase sequence with a T7 promotor, which were modified based on the luciferase T7 control DNA in the kit. TNT® Quick Master Mix, 1mM Methionine, and plasmid DNA templates (T7-luciferase, T7-luciferase-PER2-3'UTR, T7-luciferase-CRY1-3'UTR, T7-luciferase-WFS1-3'UTR, and T7-luciferase-RRBP1-3'UTR) were mixed under RNase-free conditions. To investigate the effect of ATXN2 phase separation on translation, 2 µL of ATXN2 phase-separated condensates or an equivalent amount of all M-to-S mutant proteins (60 µM) were added. The reactions were incubated at 30°C for 1 hour, and luciferase activity was measured using the Luciferase Reporter Gene Assay Kit (YEASEN).

SunTag and fluorescence imaging

SunTag-related plasmids, including pcDNA4TO-24×GCN4-v4-24×PP7 and pHR-scFv-GCN4-sfGFP-GB1 were kindly provided by Dr. Weirui Ma from Zhejiang University. The coding sequences and 3' untranslated region (UTR) of the *PER2* mRNA were

inserted into the pcDNA4TO-24×GCN4-v4-24×PP7 backbone to generate the pcDNA4TO-24×GCN4-PER2_3UTR-24×PP7 plasmid. The ATXN2 coding sequence was also cloned into the pLVX vector with an mCherry tag fused to its N-terminus, resulting in the pLVX-mCherry-ATXN2 plasmid. To visualize the co-localization of ATXN2 puncta and PER2 nascent peptide in live cells, U2OS cells were transfected with pLVX-mCherry-ATXN2, pcDNA4TO-24×GCN4-PER2_3UTR-24×PP7, and pH-R-sFv-GCN4-sfGFP-GB1 for 12 hours. The cells used for PER2 translation observation were subsequently treated with 1 µg/mL of doxycycline for 6 hours. To confirm that the observed GFP signals corresponded to translation events, 100 µg/mL of the translation inhibitor puromycin was added to the culture medium during continuous live cell imaging. Images were captured using the Olympus IXplore spinning disk microscope.

Bioluminescence Recording

The U2OS PER2:LUC cell line was kindly provided by Dr. Eric Erquan Zhang from the National Institute of Biological Sciences, Beijing (NIBS). To generate ATXN2 KD, ATXN2L KD, and ATXN2/2L double KD cells, pX459 plasmids with ATXN2/2L KO single-guide RNA (sgRNA) were transfected into U2OS PER2:LUC cells. Then the recombinant DNA, pLVX-EGFP-ATXN2-FL and pLVX-EGFP-ATXN2-LCD3 were transfected into ATXN2/2L double KD cells for rescue experiments. The cells were grown in 35 mm dishes and synchronized with 200 nM DXMS. The culture medium was replaced by a recording medium containing 100 mM luciferin for the recording of bioluminescence. Data were collected in a LumiCycle luminometer at 36°C for 3–4 days. The data, excluding the first 24-h cycle, were analyzed with the LumiCycle Analysis software, as previously described.¹⁰

Lentiviral production

HEK293T cells were utilized to produce lentiviral particles following established protocols employing second-generation packaging plasmids (pMD2.G and psPAX2). Lentiviral backbone and packaging plasmids (pLVX-EGFP-ATXN2-WT and pLVX-EGFP-ATXN2-ΔLCD3) were transfected into HEK293T cells, and the lentivirus-containing medium was harvested after 24 hours. Viral supernatant was collected and filtered through a 0.45 µm filter to remove cellular debris. Lentivirus was added to ATXN2/2L double knockout cells for 2 days after plating. GFP-positive cells were then selected using a flow cytometer.

Adeno-associated viruses (AAV) packaging and stereotaxic surgery

The AAV particles were prepared using a protocol previously described before.⁵³ The plasmids used for packaging the AAV particles included pHelper plasmid, AAV8 capsid encoding plasmid, and the pAAV-hSyn-mCherry-IRES-Cre, were obtained as gifts from Dr. Yingqing Li at Tsinghua University. The pAAV plasmid containing the rAAV genome was packaged into an AAV8 capsid via triple transient transfection by polyethylenimine. The viruses were harvested 6 days after transfection and purified by iodixanol density gradients. The AAV particles were then concentrated in an Amicon filter device and tittered by real-time PCR.

For stereotaxic surgery, animals were anesthetized with isoflurane and placed in a stereotaxic apparatus. The 300 nL of AAV8-mCherry-IRES-Cre virus (~1×10¹² vg/mL) was injected into the SCN at specific anatomical coordinates (ML: ± 0.25 mm, AP: -0.40 mm, DV: 5.75 mm), depending on the experimental paradigm. The injection was performed using a glass cannula and a microinjection pump, with a flow rate of 100 nL/min into each hemisphere sequentially. The glass cannula was left in place for 10 minutes and was completely withdrawn 10 minutes after viral delivery. The animals were tested at least two weeks later following virus injection to ensure optimal transgene expression. The proper viral expression in the SCN was confirmed post hoc using histology.

Behavioral analysis of mouse locomotor activity rhythms

To monitor the circadian rhythm of locomotor activity, mice aged 8 to 12 weeks were housed individually in cages equipped with a wheel, which were placed inside light-tight boxes. The mice were acclimated to a 12-hour light/12-hour dark photoperiod (LD 12:12) with lights on at 7 am (ZT0) and lights off at 7 pm (ZT12) for a minimum of 7 days before the start of the experiments. Ad libitum food and water were provided. The behavioral rhythms were recorded for at least 7 days in LD and 14 days in constant darkness (DD). Actograms, χ² periodogram, and Fast Fourier transform (FFT) power spectral analyses were performed using ClockLab software (Actimetrics, Wilmette, IL). The χ² periodogram was performed at 1-minute resolution over the 5–36 hour period range in LD or DD. The FFT was performed in DD as a power spectrum normalized over the range of 0 to 48 hours/cycle. The effects of genotype on period lengths and amplitudes in FFT were analyzed using unpaired t-tests.

Open Field Test

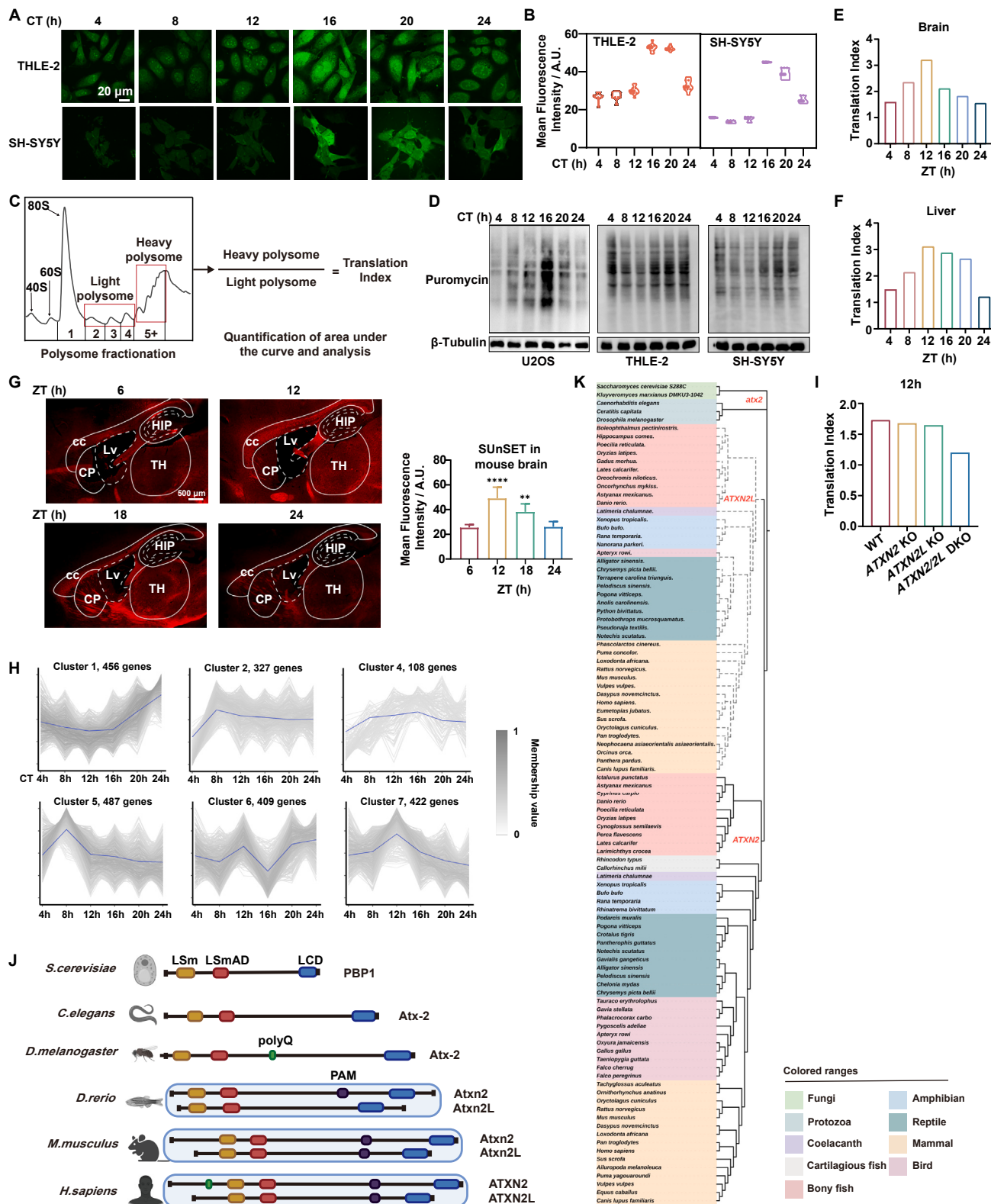
Animal behavior in the open field was recorded using an automated system, EthoVision XT14 (Noldus; TSE Multi-Conditioning System, TSE Systems). The open field test apparatus was a box measuring 50 cm × 50 cm × 50 cm, and a 300 lux light intensity was applied to the central area. The central area was defined as a 15 cm × 15 cm square in the center of the box, while the rest of the box was defined as the peripheral area. Mice were introduced into the corner of the open field box and allowed to explore for 10 minutes. Between each session, the open field test apparatus was cleaned with 70% alcohol to remove odors. The EthoVision XT14 software was used to measure parameters such as the total distance traveled and the time spent in the central area of the open field during the last 5 minutes of each session.

QUANTIFICATION AND STATISTICAL ANALYSIS

The plots were generated using GraphPad Prism software, unless otherwise stated. The R packages used in the analysis are indicated in their respective methods sections, along with the statistical tests employed. Unless otherwise specified, all statistical tests were performed using GraphPad Prism software. The unpaired t-test was utilized for comparing two groups.

To quantify the results of western blot analysis, open-source ImageJ software was used. The normalized intensities, represented as bar graphs, were calculated by comparing the intensity of the proteins of interest to that of Tubulin.

Supplemental figures



(legend on next page)

Figure S1. ATXN2 and ATXN2L together regulate the rhythmic translation, related to Figure 1

(A) HPG fluorescent staining results showing protein synthesis activity in THLE-2 and SH-SY5Y cells at different time points. Cells were synchronized, pulse-labeled with HPG for 30 min, fixed, and subjected to Click-iT HPG reaction using the Alexa-fluor 488-azide capture agent at designated time points. Scale bars, 20 μ m.

(B) Corresponding quantification of the mean HPG fluorescence intensity in (A). Values represent mean \pm SD ($n = 4$).

(C) Strategy for quantifying the translation profiles using the area under the curve calculated from heavy and light fractions. The translation index was the ratio of the area associated with heavy to light fractions.

(D) Representative immunoblot of newly synthesized polypeptide labeled by puromycin in U2OS, THLE-2, and SH-SY5Y cells.

(E and F) Quantitation of polysome fraction profile with translation index in Figures 1E and 1F.

(G) Representative images of nascent proteins labeled by puromycin in brain regions around the lateral ventricle (Lv). Puromycin was injected stereotactically into the left lateral ventricle, and sagittal brain sections were stained with puromycin antibody. Fluorescence intensities of caudoputamen (CP), thalamus (TH), corpus callosum (cc), hippocampal region (HIP) regions were measured using ImageJ (right). Values were shown as mean \pm SD (**p < 0.00005 by t test).

(H) Clusters, except for cluster 3 (Figure 1H), of the total protein with different expression patterns along the circadian rhythm were analyzed using the fuzz c-means clustering algorithm.

(I) Quantitation of polysome fraction profile with translation index in Figure 1J.

(J) Domain structures of ATXN2 and ATXN2L in representative species. The domains were colored yellow for Lsm, red for LsmAD, green for polyQ repeat, purple for PAM, and blue for the low-complexity domain (LCD).

(K) The phylogenetic tree of ATXN2 and ATXN2L indicates that ATXN2 and ATXN2L evolved from a common ancestor of atx2 in yeast and insect.

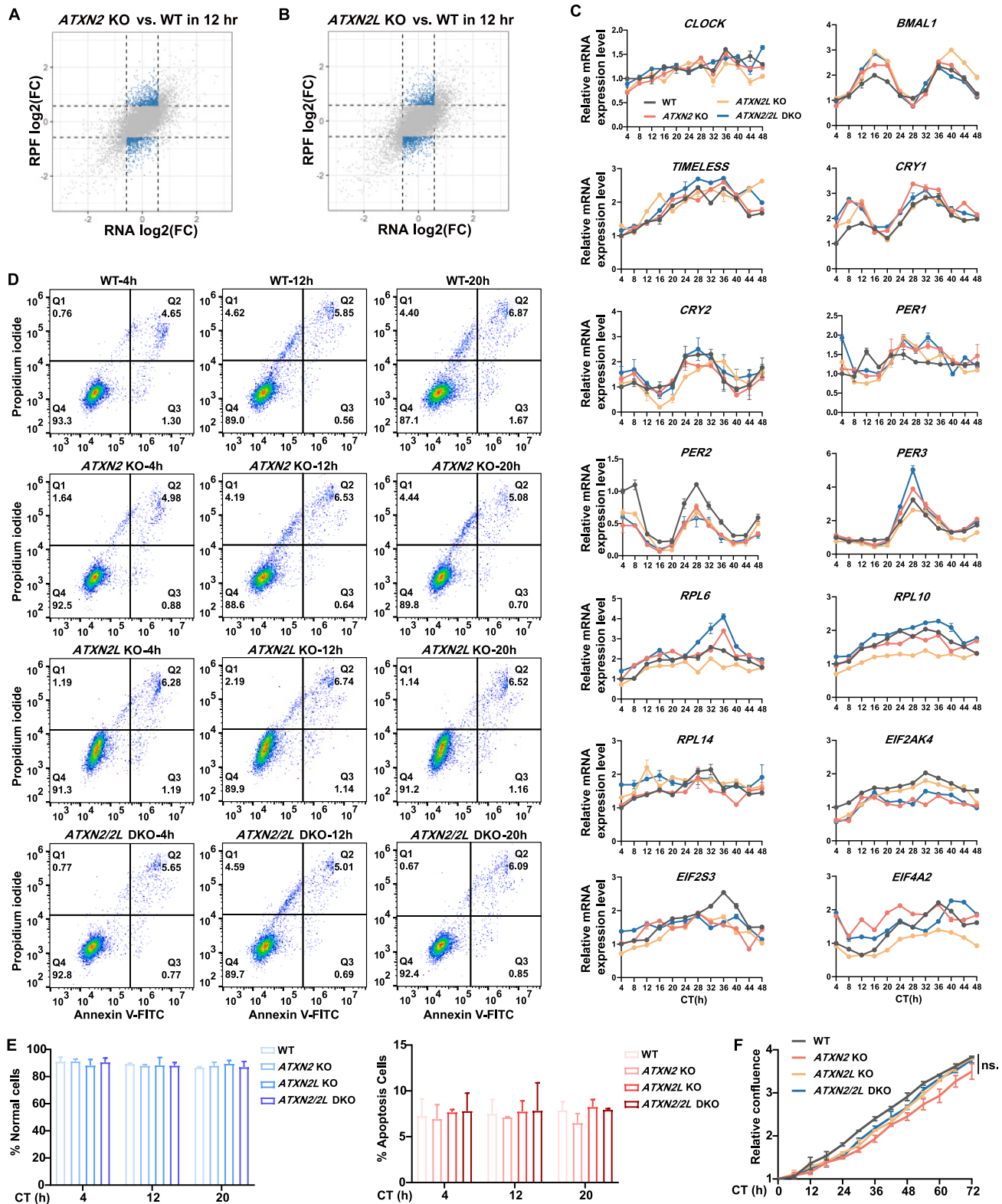


Figure S2. *ATXN2* and *ATXN2L* deficiency does not lead to changes in apoptosis or cell cycle, related to Figure 2

(A and B) Scatterplots depicting the changes in translation-level (y axis) in response to transcriptome-level changes (x axis). (A) and (B) showed the changes in *ATXN2* KO cells and *ATXN2L* KO cells compared with WT cells at 12 h.

(legend continued on next page)

(C) Quantitative analysis of RNA levels of clock-related molecules, three ribosome components, and three translation initiation factors in U2OS cells with wild type (WT), ATXN2 knockout (KO), ATXN2L KO, and ATXN2/2L double-knockout (DKO) at different time points after synchronization. The values were normalized to actin and converted to the relative expression level of the first sample of WT cells.

(D) A quadrant dot plot showing apoptosis assessed using flow cytometry after Annexin V/PI staining in U2OS cells with WT, ATXN2 KO, ATXN2L KO, and ATXN2/2L DKO along the circadian rhythm, and the percentage of apoptotic cells was determined.

(E) Diagram showing the quantification of percentage of normal (left) and apoptotic cells (right) in (D). The data were expressed as mean \pm SD.

(F) Cell proliferation of U2OS cells with WT, ATXN2 KO, ATXN2L KO, and ATXN2/2L DKO was monitored for 3 days to determine the impact of ATXN2 and ATXN2L knockout on cell growth.

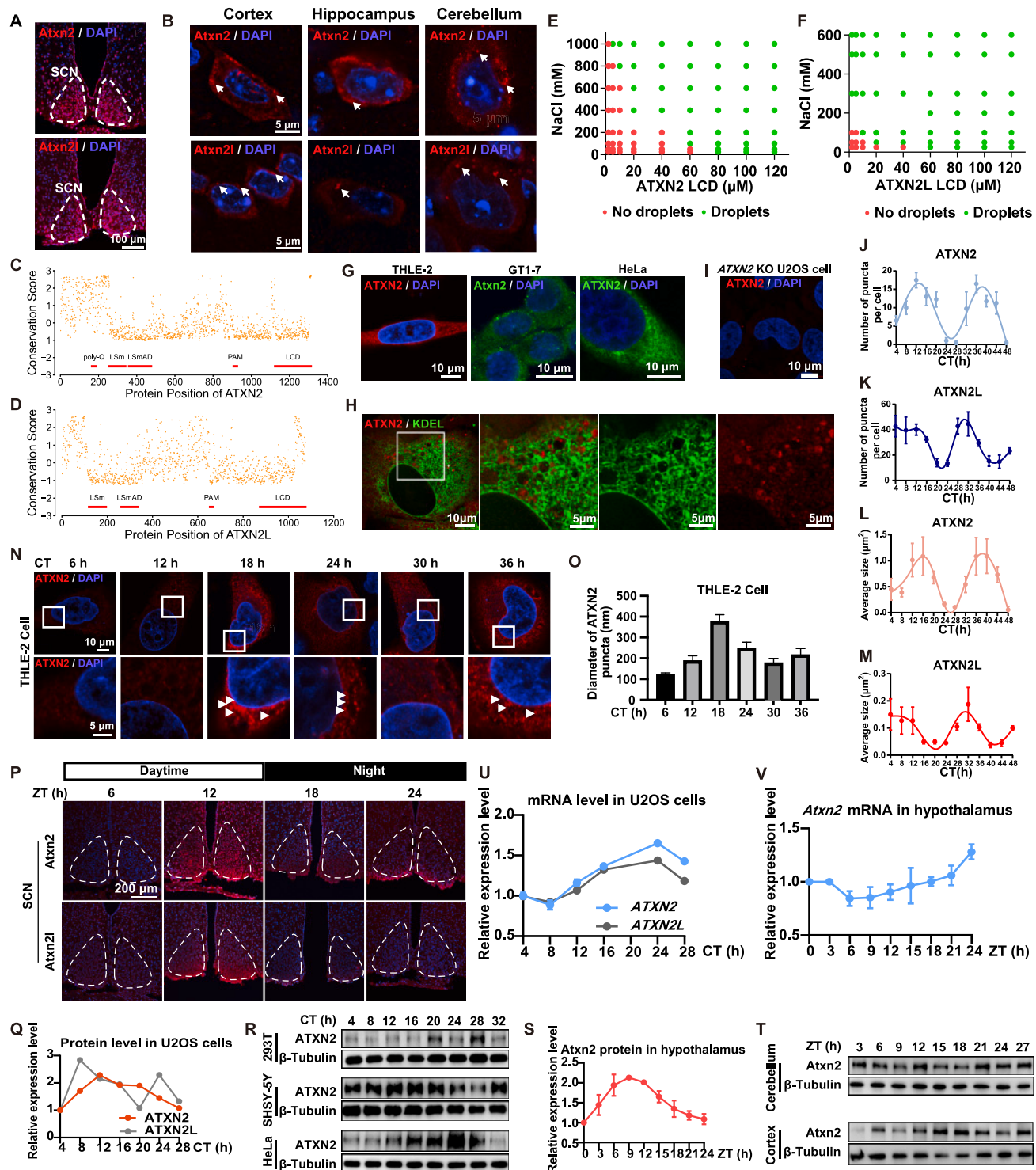


Figure S3. ATXN2 and ATXN2L phase separate in vitro and in vivo in a rhythmic manner, related to Figure 3

(A) Representative immunofluorescence images showing the subcellular localization of Atxn2 and Atxn2l (red) in the suprachiasmatic nucleus (SCN). The nuclei were stained with DAPI (blue), and the two SCNs were delineated by white dashed lines.

(B) Representative immunofluorescence images of Atxn2 and Atxn2l puncta (red) in mouse cortex, hippocampus and cerebellum regions. Nuclei were counterstained with DAPI (blue). Scale bars, 5 μm.

(C and D) Scatterplot showing the amino acid conservation of ATXN2 and ATXN2L. Lower conservation scores indicated more conserved sequences. The protein domains, including polyQ, LSm, LSmAD, PAM, and LCD, were delineated by red lines.

(legend continued on next page)

- (E and F) Phase diagram showing the ATXN2 (E) and ATXN2L (F) LCDs, respectively. The green dots indicated the occurrence of phase separation at designated conditions, while the red dots represented no phase separation.
- (G) Representative immunofluorescence images of ATXN2 puncta formation (red or green) in various cell lines including THLE-2, GT1-7, and HeLa cells. Nuclei were counterstained with DAPI (blue). Scale bars, 10 μ m.
- (H) Localization of ATXN2 condensates relative to the endoplasmic reticulum (ER). ER was stained using anti-KDEL antibody (green), while ATXN2-mCherry was shown in red. The scale bars represent 10 and 5 μ m.
- (I) Immunostaining of ATXN2 in ATXN2 knockout U2OS cells, used as a negative control.
- (J–M) Quantitative analysis of the number and average size of ATXN2 and ATXN2L puncta in Figure 3H, along a circadian cycle.
- (N) Confocal microscopy images of ATXN2 in THLE-2 cells at different circadian time points were presented. The immunostained ATXN2 was displayed in red, and magnified images were indicated with a white square box. The white triangle highlighted the ATXN2 puncta. The scale bars represent 10 and 5 μ m, respectively.
- (O) Statistical analysis of the diameters of ATXN2 puncta in (N) at different time points.
- (P) Confocal microscopy images of Atxn2 and Atxn2l (red) in the suprachiasmatic nuclei (SCNs) at different zeitgeber times (ZTs) are shown. The SCNs were circled in white dashed lines. Scale bars, 200 μ m.
- (Q) Quantitative analysis of ATXN2/2L protein levels in U2OS cells along a circadian cycle.
- (R) The abundance of ATXN2 protein oscillated in HEK293T cells, SHSY-5Y cells, and HeLa cells along the circadian cycle. ATXN2 and β -tubulin proteins were detected by western blots (WBs) at different time points with a 4-h interval over 32 h after synchronization.
- (S) Quantitative analysis of Atxn2 protein level in the hypothalamus along a circadian cycle.
- (T) The abundance of Atxn2 protein oscillated in the mouse cerebellum and cortex. Animals housed in the normal light-dark cycle were used for tissue collection at different time points with a 3-h interval. Zeitgeber time (ZT) 0 represented the time of turning on the light. β -tubulin was used as a protein loading control.
- (U and V) Quantitative analysis of ATXN2/2L RNA in U2OS cells (U) and Atxn2 RNA in the hypothalamus (V), respectively, along a circadian cycle. Each value was normalized to actin and converted to the relative expression level of the first sample.

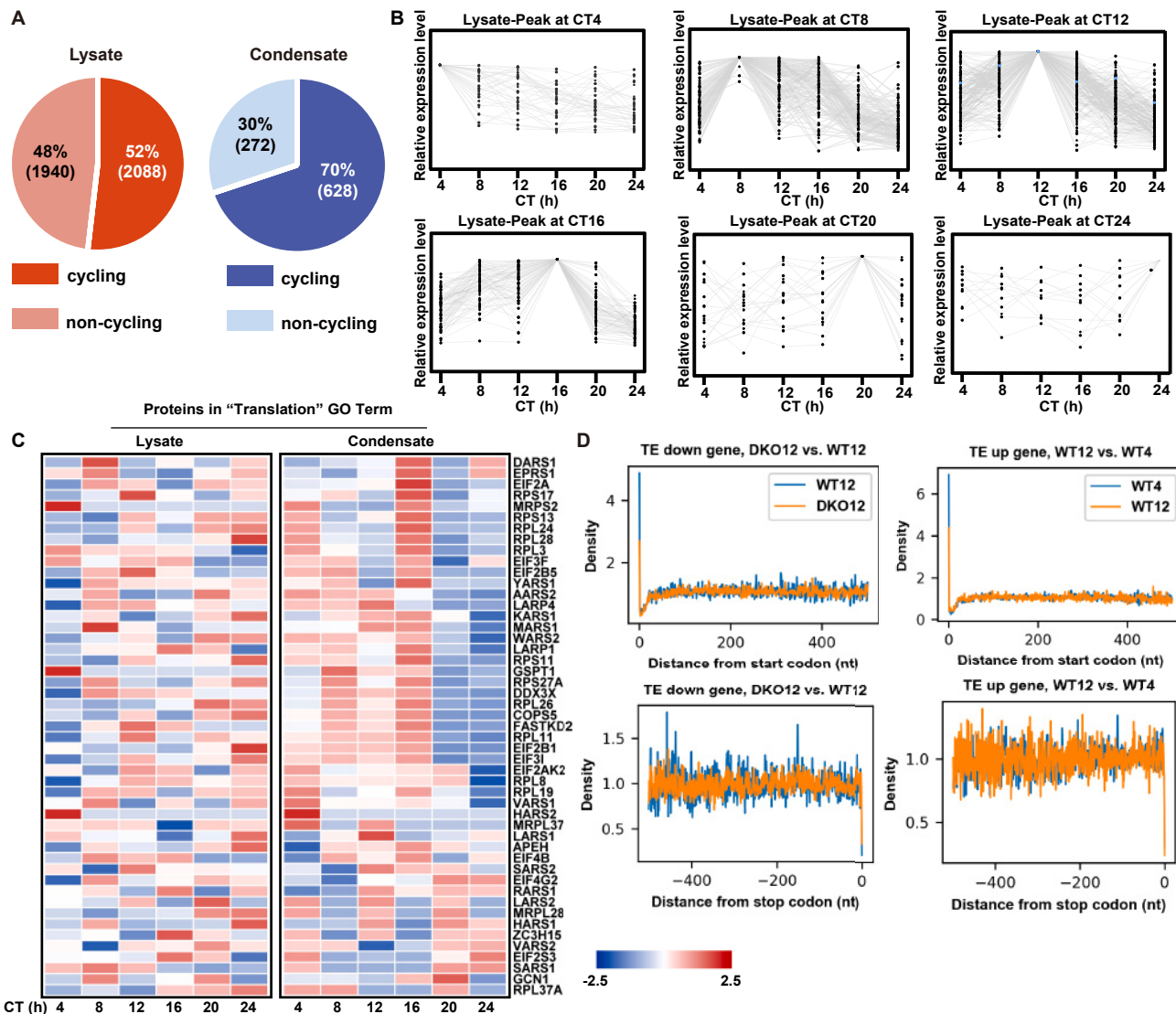


Figure S4. ATXN2 condensates oscillate and interact with translation-related proteins in a rhythmic manner, related to Figure 4

(A) Pie charts depicting the percentages of cycling and non-cycling proteins. RAIN time series periodic analysis was performed with a period of 24 h and a significance level of $p < 0.05$ to identify cycling and non-cycling proteins in cell lysate and ATXN2 condensate groups.

(B) Expression patterns of cycling proteins in the ATXN2 immunoprecipitated group. The time point of peak expression was used to classify the proteins (p value < 0.05).

(C) Heatmap showing the distribution of protein abundance for the “translation” term in the gene ontology biological process annotations at different time points.

(D) Ribosome density distribution along the CDS region of merged transcripts of which TE was upregulated from 4 to 12 h (right) and downregulated in ATXN2/2L DKO cells compared with WT cells at 12 h (left). Top: ribosome density after the start codon. Bottom: ribosome density before the stop codon.

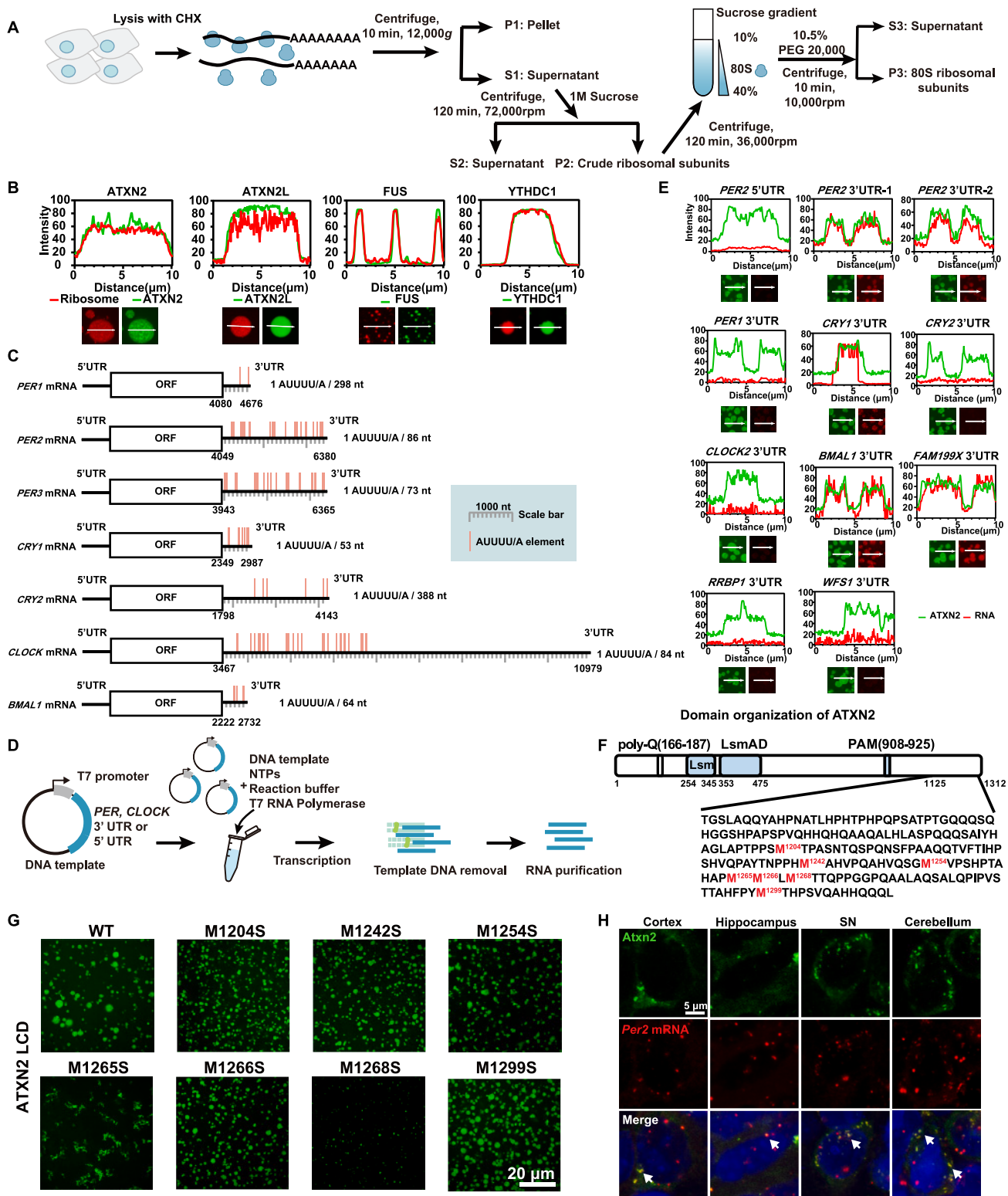


Figure S5. ATXN2 condensates recruit ribosome and clock-related mRNA, related to Figure 5

(A) Schematic workflow of the 80S ribosomal subunit purification process.

(B) The corresponding quantification of ribosome enrichment in each condensate in Figure 5A. White arrows were drawn across the condensate to indicate the analyzed sections.

(legend continued on next page)

-
- (C) The mRNA 3' UTR of core clock genes was enriched with AUUUU/A motifs, as represented in a schematic diagram.
- (D) Experimental workflow of *in vitro* transcription.
- (E) The corresponding quantification of ribosome enrichment in each condensate in [Figure 5C](#). White arrows were drawn across the ATXN2 condensate to indicate the analyzed sections.
- (F) ATXN2 LCD was rich in methionine residues, which were highlighted in red. The numbers of all methionine residues were formatted as superscripts.
- (G) Representative images showing the *in vitro* phase separation state of ATXN2 LCD proteins, including seven single M-to-S mutants. Proteins were diluted to a final concentration of 80 µM. Scale bars, 20 µm.
- (H) Representative images showed the co-localization of *Per2* mRNA and Atxn2 protein condensates in the cortex, hippocampus, substantia nigra (SN), and cerebellum, respectively. The co-localized Atxn2 puncta and *Per2* mRNAs were indicated with white arrows. Atxn2 protein was shown in green, while *Per2* mRNA was in red. Nuclei were labeled with DAPI (blue). Scale bars, 5 µm.

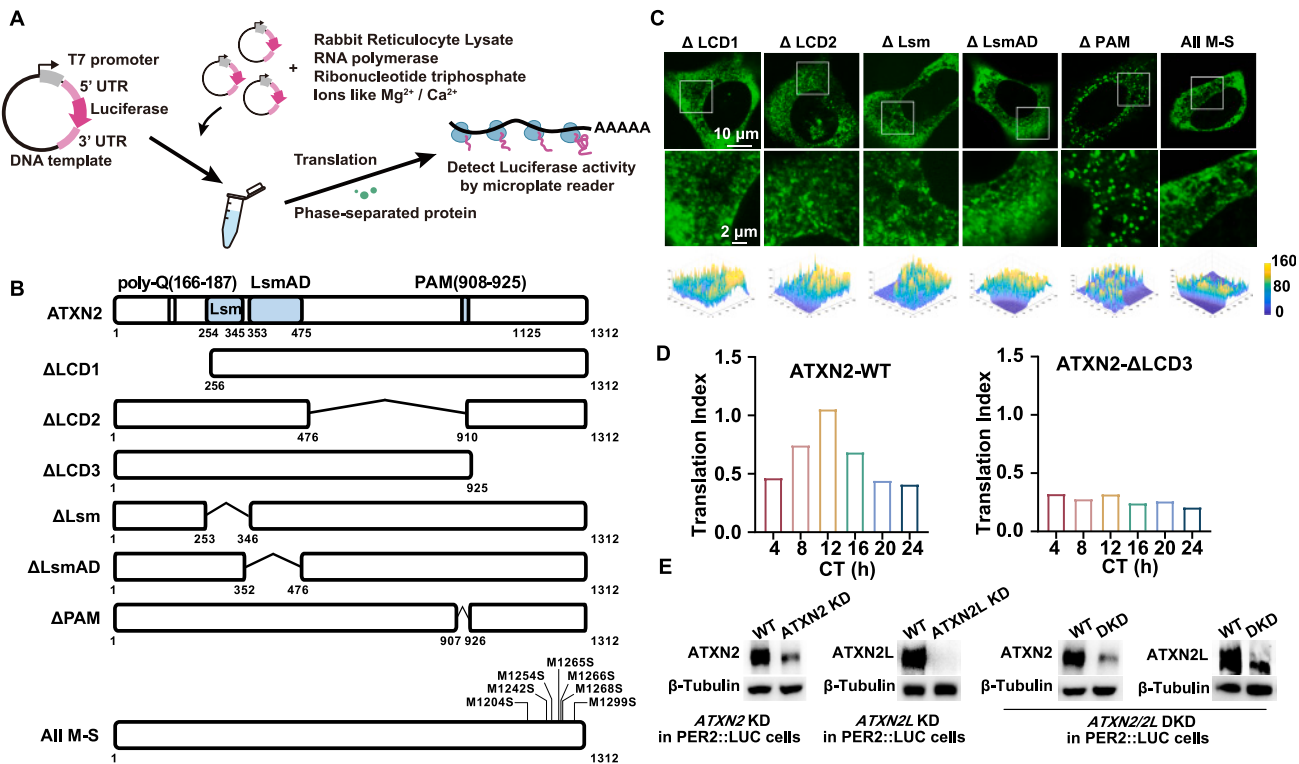
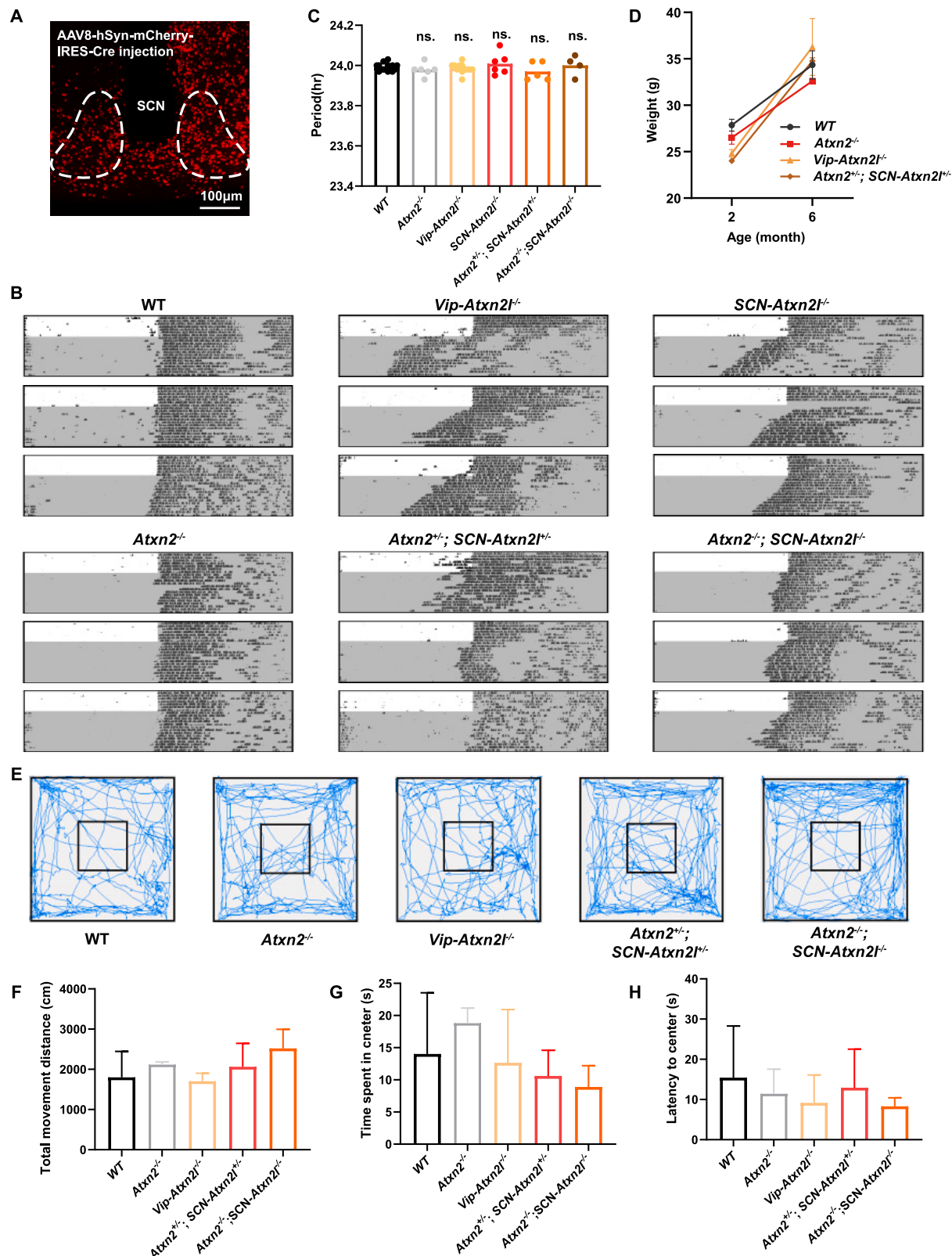


Figure S6. ATXN2 phase separation is crucial for rhymic translation, related to Figure 6

- (A) Experimental workflow of the *in vitro* translation experiment.
- (B) Domain organization of different ATXN2 mutants.
- (C) Representative images of EGFP-ATXN2 mutants except ΔLCD3 rescued in double-KO cells. A three-dimensional statistical graph of the gray value (bottom) was shown corresponding to the image. Scale bars, 10 and 2 μ m, respectively.
- (D) Quantitation of polysome fraction profile with translation index in Figure 6E.
- (E) Western blot results showing the knockdown efficiency of ATXN2 and ATXN2L in PER2::LUC U2OS cells, with β -tubulin used as a control.



(legend on next page)

Figure S7. Atxn2 and Atxn2l co-regulate circadian rhythm behavior, related to Figure 7

(A) Representative image of suprachiasmatic nucleus (SCN) showing the mCherry expression after stereotaxic injection of AAV-hSyn-mCherry-IRES-Cre for 2 weeks.

(B) The representative single-plotted actograms of voluntary wheel-running activity of different genetic modified mice. Mice were housed in 12L:12D for 7 days, followed by a shift to constant darkness for 14 days. White shading indicates lights on, while gray shading represents lights off.

(C) Average circadian free-running periods (mean \pm SD) were measured in LD conditions over 7 days from the same animals presented in Figure 7D, and statistical analysis was performed using a two-tailed t test. No significant difference was observed (ns, not significant).

(D) Body weight curves of male WT, *Atxn2*^{-/-}, *Vip-Atxn2l*^{-/-}, and *Atxn2*^{+/-}; *SCN-Atxn2l*^{+/-} compound heterozygous knockout mice.

(E) Representative trajectory plot of WT and genetically modified mice during the last 5 min of one trial in the open field test.

(F) Total movement distance was recorded and analyzed in the open field test. All data were presented as mean \pm SD.

(G and H) Latency to center zone (G) and time spent in center (H) were recorded and analyzed in the open field test. Data were presented as mean \pm SD.